*Astronomy & Astrophysics* manuscript no. output
March 17, 2025



# Euclid Quick Data Release (Q1)

## Combined *Euclid* and *Spitzer* galaxy density catalogues at $z$>1.3 and detection of significant *Euclid* passive galaxy overdensities in *Spitzer* overdense regions

Euclid Collaboration: N. Mai[1,2], S. Mei⋆[1,2], C. Cleland[1], R. Chary[3,4], J. G. Bartlett[1], G. Castignani[5], H. Dannerbauer[6], G. De Lucia[7], F. Fontanot[7,8], D. Scott[9], S. Andreon[10], S. Bhargava[11], H. Dole[12], T. Dussere[12], S. A. Stanford[13], V. P. Tran[1,2], J. R. Weaver[14], P.-A. Duc[15], I. Risso[16], N. Aghanim[12], B. Altieri[17], A. Amara[18], N. Auricchio[5], H. Aussel[19], C. Baccigalupi[8,7,20,21], M. Baldi[22,5,23], A. Balestra[24], S. Bardelli[5], P. Battaglia[5], A. Biviano[7,8], A. Bonchi[25], D. Bonino[26], E. Branchini[27,28,10], M. Brescia[29,30], J. Brinchmann[31,32], A. Caillat[33], S. Camera[34,35,26], G. Cañas-Herrera[36,37,38], V. Capobianco[26], C. Carbone[39], J. Carretero[40,41], S. Casas[42], M. Castellano[43], S. Cavuoti[30,44], K. C. Chambers[45], A. Cimatti[46], C. Colodro-Conde[47], G. Congedo[48], C. J. Conselice[49], L. Conversi[50,17], Y. Copin[51], F. Courbin[52,53], H. M. Courtois[54], A. Da Silva[55,56], H. Degaudenzi[57], A. M. Di Giorgio[58], M. Douspis[12], F. Dubath[57], C. A. J. Duncan[49], X. Dupac[17], S. Dusini[59], A. Ealet[51], S. Escoffier[60], M. Farina[58], R. Farinelli[5], F. Faustini[43,25], S. Ferriol[51], F. Finelli[5,61], P. Fosalba[62,63], S. Fotopoulou[64], M. Frailis[7], E. Franceschi[5], M. Fumana[39], S. Galeotta[7], K. George[65], B. Gillis[48], C. Giocoli[5,23], J. Gracia-Carpio[66], B. R. Granett[10], A. Grazian[24], F. Grupp[66,65], S. V. H. Haugan[67], W. Holmes[68], F. Hormuth[69], A. Hornstrup[70,71], P. Hudelot[72], K. Jahnke[73], M. Jhabvala[74], E. Keihänen[75], S. Kermiche[60], A. Kiessling[68], B. Kubik[51], M. Kümmel[65], M. Kunz[76], H. Kurki-Suonio[77,78], Q. Le Boulc'h[79], A. M. C. Le Brun[80], D. Le Mignant[33], S. Ligori[26], P. B. Lilje[67], V. Lindholm[77,78], I. Lloro[81], G. Mainetti[79], D. Maino[82,39,83], E. Maiorano[5], O. Mansutti[7], O. Marggraf[84], M. Martinelli[43,85], N. Martinet[33], F. Marulli[86,5,23], R. Massey[87], S. Maurogordato[11], E. Medinaceli[5], Y. Mellier[88,72], M. Meneghetti[5,23], E. Merlin[43], G. Meylan[89], A. Mora[90], M. Moresco[86,5], L. Moscardini[86,5,23], R. Nakajima[84], C. Neissner[91,41], S.-M. Niemi[36], J. W. Nightingale[92], C. Padilla[91], S. Paltani[57], F. Pasian[7], K. Pedersen[93], W. J. Percival[94,95,96], V. Pettorino[36], S. Pires[19], G. Polenta[25], M. Poncet[97], L. A. Popa[98], L. Pozzetti[5], F. Raison[66], A. Renzi[99,59], J. Rhodes[68], G. Riccio[30], E. Romelli[7], M. Roncarelli[5], R. Saglia[65,66], Z. Sakr[100,101,102], D. Sapone[103], B. Sartoris[65,7], J. A. Schewtschenko[48], P. Schneider[84], M. Scodeggio[39], A. Secroun[60], G. Seidel[73], M. Seiffert[68], S. Serrano[62,104,63], P. Simon[84], C. Sirignano[99,59], G. Sirri[23], L. Stanco[59], J. Steinwagner[66], P. Tallada-Crespí[40,41], A. N. Taylor[48], H. I. Teplitz[3], I. Tereno[55,105], R. Toledo-Moreo[106], F. Torradeflot[41,40], I. Tutusaus[101], L. Valenziano[5,61], J. Valiviita[77,78], T. Vassallo[65,7], G. Verdoes Kleijn[107], A. Veropalumbo[10,28,27], Y. Wang[3], J. Weller[65,66], A. Zacchei[7,8], G. Zamorani[5], F. M. Zerbi[10], E. Zucca[5], V. Allevato[30], M. Ballardini[108,109,5], M. Bolzonella[5], E. Bozzo[57], C. Burigana[110,61], R. Cabanac[101], A. Cappi[5,11], D. Di Ferdinando[23], J. A. Escartin Vigo[66], L. Gabarra[111], W. G. Hartley[57], J. Martín-Fleitas[90], S. Matthew[48], N. Mauri[46,23], R. B. Metcalf[86,5], A. Pezzotta[112,66], M. Pöntinen[77], C. Porciani[84], V. Scottez[88,113], M. Sereno[5,23], M. Tenti[23], M. Viel[8,7,21,20,114], M. Wiesmann[67], Y. Akrami[115,116], S. Alvi[108], I. T. Andika[117,118], S. Anselmi[59,99,119], M. Archidiacono[82,83], F. Atrio-Barandela[120], D. Bertacca[99,24,59], M. Bethermin[15], A. Blanchard[101], L. Blot[121,80], H. Böhringer[66,122,123], S. Borgani[124,8,7,20,114], M. L. Brown[49], S. Bruton[125], A. Calabro[43], F. Caro[43], C. S. Carvalho[105], T. Castro[7,20,8,114], Y. Charles[33], F. Cogato[86,5], A. R. Cooray[126], O. Cucciati[5], S. Davini[28], F. De Paolis[127,128,129], G. Desprez[107], A. Díaz-Sánchez[130], J. J. Diaz[6,47], S. Di Domizio[27,28], J. M. Diego[131], P. Dimauro[43,132], A. Enia[22,5], Y. Fang[65], A. G. Ferrari[23], A. Finoguenov[77], A. Fontana[43], A. Franco[128,127,129], K. Ganga[1], J. García-Bellido[115], T. Gasparetto[7], V. Gautard[133], E. Gaztanaga[63,62,134], F. Giacomini[23], F. Gianotti[5], A. H. Gonzalez[135], G. Gozaliasl[136,77], M. Guidi[22,5], C. M. Gutierrez[137], A. Hall[48], C. Hernández-Monteagudo[138,47], H. Hildebrandt[139], J. Hjorth[93], J. J. E. Kajava[140,141], Y. Kang[57], V. Kansal[142,143], D. Karagiannis[108,144], K. Kiiveri[75], C. C. Kirkpatrick[75], S. Kruk[17], J. Le Graet[60], L. Legrand[145,146], M. Lembo[108,109], F. Lepori[147], G. Leroy[148,87], G. F. Lesci[86,5], J. Lesgourgues[42], L. Leuzzi[86,5], T. I. Liaudat[149], A. Loureiro[150,151], J. Macias-Perez[152], G. Maggio[7], E. A. Magnier[45], C. Mancini[39], F. Mannucci[153], R. Maoli[154,43], C. J. A. P. Martins[155,31], L. Maurin[12], M. Miluzio[17,156], C. Moretti[21,114,7,8,20], G. Morgante[5], K. Naidoo[134], A. Navarro-Alsina[84], S. Nesseris[115], F. Passalacqua[99,59], K. Paterson[73], L. Patrizii[23], A. Pisani[60,157], D. Potter[147], S. Quai[86,5], M. Radovich[24], P.-F. Rocci[12], S. Sacquegna[127,128,129], M. Sahlén[158], D. B. Sanders[45], E. Sarpa[21,114,20], C. Scarlata[159], A. Schneider[147], D. Sciotti[43,85], E. Sellentin[160,38], F. Shankar[161], L. C. Smith[162],

K. Tanidis[111], G. Testera[28], R. Teyssier[157], S. Tosi[27, 28, 10], A. Troja[99, 59], M. Tucci[57], C. Valieri[23], A. Venhola[163], D. Vergani[5], G. Verza[164], P. Vielzeuf[60], and N. A. Walton[162]

*(Affiliations can be found after the references)*

March 17, 2025

**ABSTRACT**

The *Euclid* spacecraft will detect tens of thousands of clusters and protoclusters at $z > 1.3$ over the course of its mission. With a total coverage of 63.1 deg$^2$, the Euclid Quick Data Release 1 (Q1) is large enough to detect tens of clusters and hundreds of protoclusters at these early epochs. The Q1 photometric redshift catalogue enables us to detect clusters out to $z \lesssim 1.5$; however, infrared imaging from the *Spitzer* Space Telescope extends this limit to higher redshifts by using high local projected densities of *Spitzer*-selected galaxies as signposts for cluster and protocluster candidates. We use *Spitzer* imaging of the Euclid Deep Fields (EDFs) to derive densities for a sample of *Spitzer*-selected galaxies at redshifts $z > 1.3$, building *Spitzer* IRAC1 and IRAC2 photometric catalogues that are 95% complete at a magnitude limit of IRAC2 =22.2, 22.6, and 22.8 for the Euclid Deep Field South, Euclid Deep Field Fornax, and Euclid Deep Field North, respectively. We apply two complementary methods to calculate galaxy densities: (1) aperture and surface density; and (2) the $N$th-nearest-neighbour method. When considering a sample selected at a magnitude limit of IRAC2 $< 22.2$, at which all three EDFs are 95% complete, our surface density distributions are consistent among the three EDFs and with the United Kingdom Infrared Telescope Infrared Deep Sky Survey Ultra-Deep Survey blank field survey. We also considered a deeper sample at a magnitude limit of IRAC2 $< 22.8$, finding that 2% and 3% of the surface densities in the North and Fornax fields are $3\,\sigma$ higher than the average field distribution and similar to densities found in the Clusters Around Active Galactic Nuclei cluster survey. Our surface densities are also consistent with predictions from the GAlaxy Evolution and Assembly semi-analytical model. Using combined *Euclid* and ground-based $i$-band photometry from the Cosmic Dawn Survey, we show that our highest *Spitzer*-selected galaxy overdence regions, found at $z \approx 1.5$, also host high densities of passive galaxies. This means that we measure densities consistent with those found in clusters and protoclusters at $z > 1.3$, and our catalogues will allow us to extend cluster and protocluster detections to $z > 1.3$ in the EDFs.

**Key words.** Techniques: image processing – Methods: data analysis – cosmology: observations – large-scale structure of Universe – Galaxies: clusters: general, high redshift, photometry

## 1. Introduction

Galaxy clusters are ideal for studying the interactions between galaxies and their environment, enabling us to quantify the impact of local environment on the evolution of galaxy properties. At redshifts out to $z \approx 1$, the relation between star-formation rate and environment indicates that massive galaxies in dense regions, such as those found in galaxy clusters, tend to suppress their star formation, while more isolated galaxies exhibit higher star-formation rates (e.g., Gómez et al. 2003; Mei et al. 2009; Peng et al. 2010, 2012; Lemaux et al. 2019). At present, it is still unclear how this relation behaves at higher redshifts. In fact, different studies have identified cluster cores dominated by star-forming galaxies (e.g., Tran et al. 2010; Fassbender et al. 2011; Hayashi et al. 2011; Tadaki et al. 2012; Zeimann et al. 2012; Brodwin et al. 2013; Mei et al. 2015; Alberts et al. 2016; Hayashi et al. 2016; Shimakawa et al. 2018; Aoyama et al. 2022; Koyama et al. 2021; Polletta et al. 2021; Zheng et al. 2021) but also cores dominated by passive galaxies (e.g., Andreon et al. 2014; Cooke et al. 2015; Strazzullo et al. 2013; Noirot et al. 2016, 2018; Markov et al. 2020; Sazonova et al. 2020; Mei et al. 2023). Some clusters show both populations (Wang et al. 2016; Kubo et al. 2017; Strazzullo et al. 2018), and others present starbursts (Casey et al. 2015; Casey 2016; Wang et al. 2016).

Similarly, galaxy morphological type is strongly correlated with galaxy environment. Observations at low redshifts ($z < 0.5$) show that clusters predominantly host massive early-type galaxies that have evolved passively since redshifts of $z \approx 2-3$ (Stanford et al. 1998; van Dokkum & van der Marel 2007; Mei et al. 2009), while late-type galaxies are more prominent in isolated regions. This suggests a correlation between galaxy morphology and the surrounding environment, the so-called morphology-density relation (e.g., Postman et al. 2005; Dressler 1980; Mei et al. 2023). Mei et al. (2023) investigated and confirmed this relation out to $z \approx 2$; however, its behaviour at higher redshifts remains uncertain due to the paucity of statistical cluster samples at these redshifts.

The *Euclid* mission (Euclid Collaboration: Mellier et al. 2024) will dramatically advance studies of clusters and protoclusters (the groups that eventually merge into galaxy clusters by the present) by detecting tens of thousands of clusters (with masses $M > 10^{14} M_{\odot}$) and protoclusters at $z > 1.3$ (e.g., Sartoris et al. 2016; Ascaso et al. 2017), a still poorly explored redshift range when the first structures in the Universe form. These detections will benefit from *Euclid*'s high-resolution infrared imaging and grism spectroscopy, as well as multiwavelength ancillary imaging and spectroscopy. The Euclid Quick Data Release 1 (Q1) covers a combined area of 63.1 deg$^2$ (Euclid Collaboration: Aussel et al. 2025), which is large enough to detect tens of clusters and hundreds of protoclusters at these redshifts (Sartoris et al. 2016). Large uncertainties in the Q1 photometric redshifts restrict cluster detection to $z \leq 1.5$ (Bhargava et al., in prep.). However, combined space-based infrared imaging from *Euclid* and the *Spitzer* Space Telescope extends this limit to higher redshift (Wylezalek et al. 2013, 2014; Noirot et al. 2018; Mei et al. 2023).

In fact, the *Spitzer* Infrared Array Camera (IRAC, Fazio et al. 2004) has played a key role in detecting galaxy clusters across a wide range of masses and redshifts. In particular, *Spitzer*-selected galaxy overdense regions have been successfully used to identify galaxy clusters and protoclusters at redshift $z > 1.3$ (Papovich 2008; Wylezalek et al. 2013, 2014; Rettura et al. 2014; Baronchelli et al. 2016; Greenslade et al. 2018; Martinache et al. 2018; Noirot et al. 2016, 2018; Mei et al. 2023; Gully et al. 2024), using a colour selection in IRAC channel 1 ($\lambda = 3.6\,\mu$m; hereafter IRAC1) and channel 2 ($\lambda = 4.5\,\mu$m; hereafter IRAC2). This colour cut combined with an IRAC magnitude limit selects samples of massive galaxies at redshift $z > 1.3$ that are approxinatively 95% complete and 95% pure (Mei et al. 2023) up to a given mass limit, regardless of their morphological type or star-formation activity.

⋆ e-mail: mei@apc.in2p3.fr

In this paper, we complement the Q1 data with public archival *Spitzer* data. Our goal is to identify *Spitzer*-selected galaxy overdense regions at $z > 1.3$ and prepare for the detection of cluster and protocluster candidates with *Euclid* at these redshifts. We measure *Spitzer* photometry in the Q1 fields, calculate local projected galaxy densities, and publish examples of the highest-density regions that we find. Using *Euclid* and ground-based *i*-band photometry, we select passive galaxies in the same fields, and we give examples of some of our highest-density regions at $z \sim 1.5$ that also host high densities of passive galaxies, characteristic of galaxy clusters. This demonstrates the potential of our density catalogs for future detections of clusters and protoclusters at $z > 1.3$ in the Q1 fields.

The structure of the paper is as follows. Section 2 provides an overview of the *Spitzer*, *Euclid*, and ground-based observations, and of the GAlaxy Evolution and Assembly (GAEA) semi-analytical model. Section 3 describes our *Spitzer* photometric measurements. Section 4 presents the two methods used to compute the local projected galaxy densities, the final catalogues, and our density distributions. Section 5 presents our results and compares them to *Spitzer*-selected galaxy density measurements in a blank field and in a cluster survey, as well as to the predictions from the GAEA model (De Lucia & Blaizot 2007; De Lucia et al. 2024). Finally, Sect. 6 compares our density measurements to other density detections in the EDF.

Unless otherwise specified, we adopt the *Planck* 2015 (Planck Collaboration et al. 2016) flat ΛCDM cosmology, with $\Omega_{\rm m} = 0.308$, $\Omega_\Lambda = 0.692$, and $H_0 = 67.8\,{\rm km\,s^{-1}\,Mpc^{-1}}$; magnitudes are given in the AB system (Oke & Gunn 1983; Sirianni et al. 2005).

## 2. Observations and simulations

### 2.1. The Euclid Q1 release and ancillary data

The Q1 release (Euclid Collaboration: Aussel et al. 2025) focuses on the three Euclid Deep Fields (EDFs), namely, the Euclid Deep Field Fornax (EDF-F), Euclid Deep Field North (EDF-N), and Euclid Deep Field South (EDF-S). These fields were selected to minimise contamination from foreground sources, allowing for the study of high-redshift objects. The EDF-F covers $12.1\,{\rm deg}^2$, the EDF-N, $22.9\,{\rm deg}^2$, and the EDF-S, $28.1\,{\rm deg}^2$.

The Q1 data set consists of 351 tiles, each with a field of view of $0.57\,{\rm deg}^2$, corresponding to $0\fdg75 \times 0\fdg75$. These observations reach a $10\,\sigma$ magnitude limit of 24.5 in the Visible Instrument (VIS) filter, $I_{\rm E}$ (Euclid Collaboration: Cropper et al. 2024), and a $5\,\sigma$ magnitude limit of 24.5 in each of the filters of the Near Infrared Spectrometer and Photometer (NISP): $Y_{\rm E}$, $J_{\rm E}$, and $H_{\rm E}$ (Euclid Collaboration: Jahnke et al. 2024). The spatial resolution of the images is defined by a pixel scale of $0\farcs1$ for VIS and $0\farcs3$ for NISP. We focus on *Euclid* infrared observations in the $H_{\rm E}$ filter.

The Q1 release includes galaxy photometry from *Euclid* and external data, and galaxy properties obtained with the *Euclid* Science Ground Segment (SGS) Organisational Unit (OU) MER pipeline (Euclid Collaboration: Romelli et al. 2025). We use the Q1 catalogue photometric redshifts derived by the `Phosphorus` method, which were produced by OU-PHZ (Euclid Collaboration: Tucci et al. 2025). This method provides Bayesian posterior distributions of photometric redshifts. To ensure consistent data quality, we selected galaxies from the Q1 catalogue by applying detection quality flags generated by the pipeline to filter out sources that are saturated, located near image borders, affected by contamination from nearby objects, blended by other sources, or classified as spurious detections.

For the ancillary data, we use ground-based observations of the EDF-N and EDF-F from the Hyper-Suprime Cam (HSC) *i*-band (hereafter $i_{\rm HSC}$) from the Hawaii Twenty Square Degree Survey (H20), as part of the Cosmic Dawn Survey (DAWN; Euclid Collaboration: Zalesky et al. 2024). The DAWN photometric catalogue was obtained using `The Farmer` (Weaver et al. 2023), a software package designed to recover fluxes by modelling surface brightness profiles. The $5\,\sigma$ magnitude depth is $i_{\rm HSC} = 25.9$.

### 2.2. Spitzer Space Telescope observations

We use public *Spitzer* IRAC1 and IRAC2 mosaic images from Moneti et al. (2022). These images were created by combining archival data from both the pre- and post-cryogenic missions, along with legacy surveys specifically designed to enhance the coverage in the EDFs. The program IDs and details are found in Moneti et al. (2022).

The IRAC1 and IRAC2 images each cover a $5\farcm2 \times 5\farcm2$ field of view. The *Spitzer* Infrared Array Camera (IRAC) point-spread function (PSF) has a full width at half maximum of $1\farcs95$ and $2\farcs02$ in IRAC1 and IRAC2, respectively (IRAC Instrument Handbook[1]). The observations were processed and mosaiced using the `MOPEX` package (Makovoz & Khan 2005) and resampled to a pixel scale of $0\farcs6$.

The EDF-S is covered by uniform observations obtained over an area of $\approx 23.37\,{\rm deg}^2$ in both channels. The EDF-N and EDF-F include multiple reprocessed archival data sets with varying observation strategies and characteristics, resulting in inhomogeneous depth and coverage. They cover an area of approximately $11.64\,{\rm deg}^2$ and $10.79\,{\rm deg}^2$, respectively. The depth of the IRAC1 images reaches at least 24 mag at $5\,\sigma$ in a $2\farcs5$ aperture. Details of the image processing can be found in Moneti et al. (2022).

### 2.3. Simulations

The GAEA simulations are based on a semi-analytical model (De Lucia & Blaizot 2007; De Lucia et al. 2024), designed to study galaxy formation and evolution in a cosmological context by including explicit modelling of the relevant physical processes governing the evolution of the baryonic components. It is built on merger trees derived from the Millenium Simulation (Springel et al. 2005), which follow the hierarchical growth of dark matter halos and provide the structural framework for modelling baryonic processes, such as active galactic nuclei (AGN) feedback, disc instabilities, reheating and ejection efficiency in stellar feedback, and gas ram-pressure stripping from satellite galaxies.

In the following, we use a simulated light-cone that has been created for the Euclid Consortium and is based on the latest version of the GAEA model (De Lucia et al. 2024). The light cone covers a $5\fdg27$ diameter aperture, and includes approximately 6 500 000 galaxies within the redshift range $0 \leq z \leq 4$. In addition to a number of predicted physical properties, the light cone includes photometry in a large set of photometric bands, including IRAC1 and IRAC2. Although the cosmology used in GAEA differs from that used in this paper, we do not expect a significant impact on the results when comparing this model to observations (see Sect. 4).

[1] https://irsa.ipac.caltech.edu/data/SPITZER/docs/irac/iracinstrumenthandbook/5/

## 3. Photometry

### 3.1. Bright source masking

Source detection was performed using the `SourceExtractor` software (Bertin & Arnouts 1996), a widely-used tool for photometric analysis. We mask bright sources before performing photometric measurements on the *Spitzer* images. As noted by Ji et al. (2018), accurate extraction of faint sources requires precise background estimation. Given that our fields contain some bright sources, it is crucial to mask these objects to allow `SourceExtractor` (see Sect. 3.2.1) to compute the background more accurately. To achieve this, we perform an initial extraction in a so-called 'cold mode', where we identify only the brightest sources using a high detection threshold. The output aperture maps are then used to mask sources with magnitudes brighter than 17.

To account for extended or elongated objects, we employ the Kron aperture to define the mask. Although the aperture computed by `SourceExtractor` is generally sufficient, the brightest sources tend to have artifacts or to be highly extended, which contaminates the background estimation. Considering this, we follow the approach outlined by Kelvin et al. (2023) and expand the mask size by adding a number of pixels $p$ to our mask radii, with

$$p \equiv 10^{-0.2\,(m_{\rm IRAC}-17)} + 6\,, \qquad (1)$$

where $m_{\rm IRAC}$ is our catalogue magnitude computed by `SourceExtractor`. These additional pixels increase the mask size as the magnitude decreases, encompassing the extended flux of bright sources that could otherwise perturb the local background estimation and thus contaminate the flux of nearby faint sources. As a result of these masking procedures, the total area of each field is slightly reduced. We report an average areal reduction of 2.6% for the three regions through the two channels.

### 3.2. Source extraction

#### 3.2.1. `SourceExtractor`

To ensure consistent flux determination across both IRAC channels, we use `SourceExtractor` in dual mode, with IRAC1 as the detection image, and measure `MAG_AUTO` magnitudes. The images are in units of MJy sr$^{-1}$, hence we apply a zero-point magnitude of 21.58 to convert them to AB magnitudes[2]. Weight maps are provided in the public data release. We give our `SourceExtractor` configuration parameters in Table B.1, optimized by Lacy et al. (2005) for faint source detection, such as needed for high-redshift galaxies. The final photometric uncertainties are the sum in quadrature of the statistical uncertainty, the shot noise, and the uncertainty on the photometric zero point.

Figure 1 illustrates the number of detected sources as a function of IRAC1 and IRAC2 magnitudes. To asses the completeness of our catalogues, we compare our number counts to that from COSMOS2020 (Weaver et al. 2022), which has deeper *Spitzer* observations. We compute our catalogue completeness in magnitude bins by dividing our number counts by the COSMOS2020 one. Table 1 gives the magnitude limits at which our photometric catalogues are 95% complete for each Q1 field.

Our results qualitatively agree with the Moneti et al. (2022) number counts shown in their figure 8. However, we could not perform a quantitative analysis because their catalogues are not public. Also, while comparing our catalogues to COSMOS2020, we assume that COSMOS2020 is a representative catalogue for galaxy number counts, and do not take into account field-to-field variations due to sampling variance.

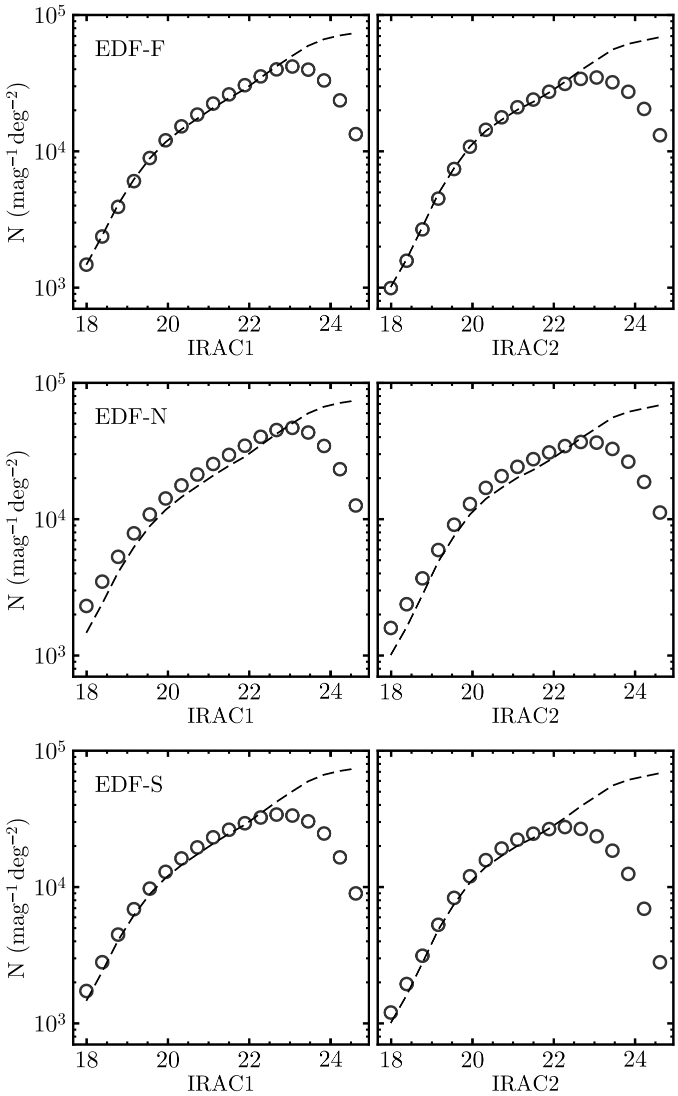


**Fig. 1.** Our catalogue number counts. We show the number of detections as a function of magnitude. The circles represent our data, while the black dashed line corresponds to the COSMOS2020 catalogue. Our catalogues yield similar number counts for EDF-F and EDF-N. However, EDF-S displays a slight deficit of faint sources, primarily because of the shallower magnitude limit. Our results are consistent with those of Moneti et al. (2022).

**Table 1.** Magnitude limits corresponding to 95% completeness for the three EDFs.

| Field | IRAC1 | IRAC2 |
|---|---|---|
| EDF-S | 22.4 | 22.2 |
| EDF-F | 22.9 | 22.6 |
| EDF-N | 23.2 | 22.8 |

[2] Considering the 0.″6 pixel size of *Spitzer*'s images.

**Table 2.** Average background aperture density $N_{\rm bkg}$ calculated at a radius $R$, and its standard deviation $\sigma_{\rm bkg}$, calculated in the SpUDS field, at the depth of S1 and S2.

| Field | Sample | $R$ | $N_{\rm bkg} \pm \sigma_{\rm bkg}$ |
|---|---|---|---|
| SpUDS | S1 | 0.′5 | 1.7 ± 0.6 |
| | | 1′ | 7.0 ± 2.2 |
| | S2 | 0.′5 | 2.4 ± 0.7 |
| | | 1′ | 9.6 ± 2.1 |

#### 3.2.2. TPHOT *Spitzer* photometry

To improve deblending of *Spitzer* galaxies, and therefore attain more precise photometry, we perform additional photometric measurements using the `t-phot` software (Merlin et al. 2015, 2016). This is specifically designed to perform photometry while accounting for source blending using higher resolution images as a reference to obtain photometry in lower resolution images of the same field. It incorporates spatial and morphological information extracted from the high-resolution image to accurately model and measure the fluxes of sources in a lower-resolution image.

The core of the `t-phot` methodology relies on constructing and solving a linear system that minimises the $\chi^2$ comparison between the observed low-resolution image pixel values and the model fluxes derived from the high-resolution priors. In this paper, we use high-resolution *Euclid* $H_{\rm E}$ images as priors to measure photometry in IRAC images. We give our `t-phot` parameters in Table B.2.

The *Euclid* input is the Q1 photometric catalogue and its associated segmentation maps (Euclid Collaboration: Romelli et al. 2025). We then apply the `t-phot` pipeline using the cell-on-object fitting method to obtain the multiwavelength photometric catalogue. The statistical uncertainty on the photometry was estimated with `t-phot`. Mei et al. (2023) have shown that for galaxies at our redshifts, Monte-Carlo simulations confirm `t-phot` estimates. The final photometric uncertainties are the sum in quadrature of the statistical uncertainty, shot noise, and the uncertainty on the photometric zero point.

## 4. Density calculation

### 4.1. Galaxy density measurements

The presence of different densities in the spatial distribution of galaxies reflects the intricate large-scale structure of the Universe. To measure projected local galaxy densities (hereafter densities), we use two methods: the aperture density; and the $N$th-nearest-neighbour methods. Both quantify the local galaxy environment.

The first method consists in measuring the number of galaxies around a given galaxy within a fixed circular aperture. The aperture density is defined as

$$\Sigma_{(r<R)} = \frac{N_{\rm gal} - N_{\rm bkg}}{N_{\rm bkg}}\,, \tag{2}$$

where $N_{\rm gal}$ is the number of galaxies within an aperture of radius $R$ from a given galaxy, and $N_{\rm bkg}$ is the mean number of background galaxies in the field within the same aperture. We adopt $R = 0.'5$ and $R = 1'$, which correspond approximately to 0.25 and 0.5 physical Mpc, respectively, in our redshift range, $z > 1.3$. These values are consistent with the aperture densities calculated by Wylezalek et al. (2014) and Mei et al. (2023).

**Table 3.** Aperture density ($\Sigma_{(r<1')}$) mean and standard deviation for the EDFs and GAEA at the depth of the the S1 and S2 samples.

| Field | Sample | Mean | Standard deviation |
|---|---|---|---|
| EDF-N | S1 | 7.1 | 2.3 |
| | S2 | 10.0 | 2.8 |
| EDF-N | S1 | 7.0 | 2.3 |
| | S2 | 9.3 | 2.8 |
| EDF-S | S1 | 6.9 | 2.2 |
| GAEA | S2 | 9.8 | 3.3 |

The associated signal-to-noise ratio (S/N) is

$$\mathrm{S/N}_{r<R} = \frac{N_{\rm gal} - N_{\rm bkg}}{\sigma_{\rm bkg}}\,, \tag{3}$$

where $\sigma_{\rm bkg}$ is the standard deviation of the background. The S/N provides a robust measure of the relative enhancement in galaxy density compared to background variations. Following Wylezalek et al. (2014), we calculate $N_{\rm bkg}$ and $\sigma_{\rm bkg}$ from the United Kingdom Infrared Telescope Infrared Deep Sky Survey Ultra-Deep Survey (SpUDS). To compare with the literature, the figures in this paper use the surface density, which is defined as the number $N_{r<R}$ of selected galaxies within a circle of radius $R$, and does not depend on background estimates. This quantity is directly proportional to $\Sigma_{(r<R)}$. We calculate the average and standard deviation of the surface density distributions by applying a 3 $\sigma$ iterative clip, which discards densities at $> 3\,\sigma$ when deriving the average density and its standard deviation, until convergence.

Following Rettura et al. (2018), we estimate the foreground star contamination using the Wainscoat et al. (1992) model,[3] which predicts the number of optical-to-infrared point sources at a given position in the sky. For EDF-F, EDF-N, and EDF-S we find an average contamination of 0.72, 1.9, and 0.9 stars per arcmin$^2$, respectively. We correct our density measurement accordingly.

The second approach is the $N$th-nearest-neighbour method, which extends the analysis to larger spatial scales by calculating the distance to the $N$th nearest-neighbour galaxy. It offers a broader perspective on galaxy density across varying scales. The density calculated with this method is defined as

$$\Sigma_N = \frac{N}{\pi D_N^2}\,, \tag{4}$$

where $N$ is the number of neighbouring galaxies and $D_N$ is the physical distance to the $N$th nearest neighbour in Mpc. Postman et al. (2005) and Mei et al. (2023) found consistent results for $N$ in the range of 5 to 10. For this paper, we adopt $N = 7$, following previous density estimates in clusters observed with the *Hubble* Space Telescope (HST; Postman et al. 2005) and in CARLA (Mei et al. 2023).

We applied these density measurements to samples of *Spitzer*-selected galaxies at $z > 1.3$, and to passive-selected galaxies from *Euclid* and ground-based $i$-band photometry from the DAWN survey. These galaxy samples are described in the next sections.

[3] http://irsa.ipac.caltech.edu/applications/BackgroundModel/

### 4.2. IRAC-selected sources

The galaxy spectral energy distribution presents an enhancement at 1.6 µm (Sawicki 2002) as a prominent feature (bump) in the near-infrared spectra of galaxies, which is generated by $H^-$ in the atmospheres of cool stars. With increasing redshift, this bump shifts progressively through the IRAC1 band and into the IRAC2 band. This spectral evolution causes galaxies in this redshift range to exhibit a higher flux in the IRAC2 band than in the IRAC1 band, resulting in a positive IRAC1−IRAC2 colour. This phenomenon enables us to use a colour cut of IRAC1 − IRAC2 > −0.1 to select samples of massive galaxies at $z > 1.3$ that are approximately 95% complete and 95% pure, regardless of their star formation activity and age (Papovich 2008; Mei et al. 2023).

Given the different magnitude limits of each EDFs (see Table 1), for homogeneity we build two different galaxy samples to calculate galaxy densities. In both cases, we apply an upper magnitude limit of IRAC2 > 18 to exclude contamination from bright stars (Wylezalek et al. 2014). Following Wylezalek et al. (2014), we also select only galaxies with a flux S/N of $S/N_f > 3.5$ to keep only the most reliable detections.

The first sample (hereafter S1) is selected at the magnitude limit of the shallowest field, EDF-S, which is IRAC2 < 22.2, at which all the EDFs fields are at least 95% complete. This selection ensures a homogeneous galaxy sample simultaneously in all three EDFs. This magnitude cut corresponds approximately to a galaxy stellar mass of $\log_{10}(M_*/M_\odot) \gtrsim 10.0 \pm 0.4$, following and adapting the calibration of Mei et al. (2023), which derives the galaxy mass from its correlation with IRAC1 magnitudes.

The second sample (hereafter S2) is selected at deeper IRAC2 magnitude limits to compare it to density measurements available in the literature. We choose this sample magnitude limit to be similar to the CARLA cluster survey and the blank field survey from the SpUDS (Galametz et al. 2013) that have been used in the literature to select clusters and protoclusters at $z > 1.3$ (Wylezalek et al. 2013, 2014).

CARLA was carried out during *Spitzer* Cycles 7 and 8 using IRAC (P.I. D. Stern). CARLA focuses on detecting galaxy cluster candidates around radio-loud quasars (RLQs) and high-redshift radio galaxies (HzRGs), because radio sources are thought to trace dense regions of the Universe at high redshifts (e.g., Hatch et al. 2014; Daddi et al. 2017). CARLA targets a sample of about 400 RLQs and HzRGs at $z > 1.3$. Wylezalek et al. (2013) found that 46% and 11% of the CARLA densities are larger than those found in the SpUDS field at a $2\sigma$ and a $5\sigma$ level, respectively. About 20 of these CARLA overdense regions are spectroscopically confirmed and classified as clusters or protoclusters (Noirot et al. 2018), and some of them show high local galaxy densities and high percentages of passive and early-type galaxies (Noirot et al. 2016; Mei et al. 2023).

SpUDS covers a field area of approximately 1 deg$^2$ and was conducted as part of the *Spitzer* Cycle 4 Legacy Program. One of the primary goals of this survey was to study galaxy environments, including the influence of local and global surroundings on galaxy properties, such as star formation and quenching. For our density measurements in SpUDS, we apply the same IRAC colour, magnitude, and S/N cuts as for the EDFs.

Since the CARLA and SpUDS fields are 95% complete at IRAC2 = 22.9, we select our second sample at a similar magnitude limit of IRAC2 = 22.8, at which the EDF-N is 95% complete. For this comparison, we will consider only EDF-N and EDF-F, which is 95% complete at IRAC2 = 22.6, while we exclude the shallower EDF-S. This magnitude cut corresponds approximately to a galaxy stellar mass of $\log_{10}(M_*/M_\odot) \gtrsim 9.5 \pm 0.4$. Table 2 gives the surface density and its standard deviation for our different samples and $R$ values.

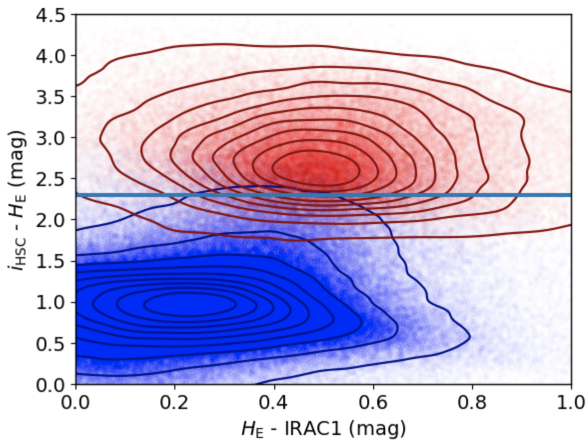


**Fig. 2.** Simulated observational ($i_{HSC}$- $H_E$) versus ($H_E$- IRAC1) colour-colour diagram for passive and star-forming galaxies from the GAEA simulations. Passive and star-forming galaxies are shown as red and blue points, respectively. The horizontal line delineates the separation between passive and star-forming galaxies adopted in this paper, with passive galaxies cut at $(i_{HSC} - H_E) = 2.3$. This simple criteria is predicted to select passive galaxy samples that are about 90% complete and 90% pure. The contours represent the percentiles of the passive and star-forming galaxy distribution, in increments of 10%. For example, the first and last contour from the centre of each distribution indicate that 10% and 90% of the galaxies, respectively, are within this contour.

### 4.3. Passive galaxy sample

The goal of this paper is to establish the basis for combining *Spitzer* and *Euclid* observations to extend the detection of clusters and protocluster candidates to redshifts $z > 1.3$. To that end, we use *Euclid* photometry from the Q1 release and our *Spitzer* photometry and densities to identify extreme *Spitzer* overdense regions that host large numbers of passive galaxies. We aim to find interesting examples of potential cluster and protocluster candidates at $z > 1.3$. A catalogue and classification of Q1 clusters and protoclusters detected using our galaxy catalogues is beyond the scope of this paper. We will pursue the necessary in-depth density distribution analysis in a future work (Mei et al., in prep.).

These examples are interesting because Mei et al. (2023) found that *Spitzer*-selected regions with high $\Sigma_7$ also show large fractions of passive galaxies out to $z \approx 2$ (see also Papovich 2008). They demonstrated that apparent-magnitude colour-colour diagrams using ground-based *i*-band observations, HST Wide Field Camera 3 (WFC3), and *Spitzer* can separate passive from star-forming galaxies at $1 < z < 2$, in the same way as the widely used rest-frame *UVJ* (Williams et al. 2009) and *NUVJ* (Arnouts et al. 2013) diagrams. In fact, the *i*-band, the WFC3 F160W (hereafter $H_{160}$), F140W (hereafter $H_{140}$), and the IRAC1 filters roughly correspond to rest-frame NUV, *V*, and *J*-band at these redshifts. Mei et al. (2023) demonstrated that these can be used to separate passive galaxies samples that are approximately 85% complete and 85% pure. A cut at high ($H_{160}$ − IRAC1) colour, typically at $(H_{160} - \mathrm{IRAC1}) \lesssim 1.6$, separates red passive galaxies from red dusty star-forming galaxies ($\lesssim 10\%$ of the red galaxies).

In EDF-N, Q1 $H_E$ photometry, combined with deep $i_{HSC}$ from the DAWN survey and IRAC1, provide apparent magnitudes that correspond to rest-frame NUV, $V$ and $J$-band at $1.3 \lesssim z \lesssim 3$. To delineate the passive galaxy region in the $(i_{\rm HSC} - H_{\rm E})$ versus $(H_{\rm E} - {\rm IRAC1})$ colour-colour diagram, we use the GAEA simulations, downgraded to the Q1, DAWN, and our IRAC1 photometric uncertainties in these filters. We start from the GAEA photometric catalogue, which does not have uncertainties, and add the $H_{\rm E}$ and $i_{\rm HSC}$ photometric uncertainties from Q1 and the DAWN survey, and our IRAC1 photometric uncertainties. We extract photometric uncertainties from the observational distributions in each band in steps of 0.05 mag. In this observational mock, we define a galaxy as quenched if the GAEA sSFR $< 0.3\, t_{{\rm H},z}^{-1}$ (Franx et al. 2008), where $t_{{\rm H},z}$ is the Hubble time. A galaxy is defined as star-forming if it has sSFR $\geq 0.3\, t_{{\rm H},z}^{-1}$.

Figure 2 shows the distribution of the simulated observational ($i_{\rm HSC}$ - $H_{\rm E}$) versus ($H_{\rm E}$- IRAC1) colour-colour diagram for passive and star-forming galaxies selected as above. The GAEA galaxy population, which does not manifest dusty star-forming galaxies, and the large uncertainties in the current Q1 and DAWN catalogues do not permit us to define the equivalent of the Williams et al. (2009) passive galaxy regions, as in Mei et al. (2023). In fact, when optimising the standard equations to separate passive from star-forming galaxies,

$$\begin{aligned} (i_{\rm HSC} - H_{\rm E}) &> y_0\,, \\ (H_{\rm E} - {\rm IRAC1}) &< x_0\,, \\ (i_{\rm HSC} - H_{\rm E}) &> a + b \times (H_{\rm E} - {\rm IRAC1})\,, \end{aligned}$$

we find that the only the first equation really matters, which efficiently separates passive from star-forming galaxies without further cuts. With $y_0 = 2.3$, we obtain a sample of passive galaxies that is approximately 90% complete and 90% pure.

Given that GAEA reproduces observations of quenched galaxies in the local Universe very well (De Lucia et al. 2024; Euclid Collaboration: Cleland et al. 2025), we apply this cut found with simulations, $(i_{\rm HSC} - H_{\rm E}) > 2.3$, to observed Q1 and DAWN apparent magnitudes to select a sample of passive galaxies that we predict to be 90% complete and 90% pure based on the GAEA simulations. We then calculate overdense regions of passive galaxies using the same methods described in Sect. 4. The average and standard deviation of the passive galaxy surface density distribution with $(R = 1')$ are $\Sigma_{r<1'} = 0.8 \pm 0.9$ at the depth of S2.

## 5. Results

### 5.1. Density distributions

We present our density measurement distributions and compare them to those published for two other relevant *Spitzer*-based surveys available in the literature: the SpUDS blank field and the CARLA cluster survey. We also compare our results to predictions from the GAEA semi-analytical model (De Lucia et al. 2024). Since the published densities are surface densities with $R = 1'$, we focus only on surface density measurements with this aperture in this section. We recall that these are densities measured around each selected galaxy, and several might belong to the same structure; however, we do not perform structure detection in this paper.

Figure 3 shows the S1 surface density distributions for the three EDFs compared to SpUDS. At the same magnitude limit of IRAC2 = 22.2, all samples are homogeneous and at least 95% complete. Table 3 lists the Gaussian mean and standard deviation of each distribution. This selection corresponds to galaxies with $\log_{10}(M_*/M_\odot) \gtrsim 10.0 \pm 0.4$ (see Sect. 4.2). For this massive

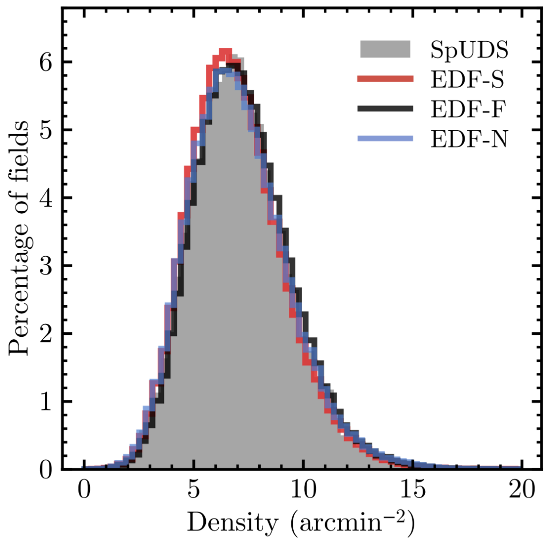


**Fig. 3.** *Spitzer* surface density distributions ($R = 1'$) for the three EDFs and SpUDS. We calculate surface densities at the same magnitude limit, IRAC2 = 22.2, where all samples are at least 95% complete. The four distributions show similar means and standard deviations (see Tables 2 and 3). The distributions in the three EDFs and in SpUDS are consistent, and typical of blank fields. Only around 1% of the surface densities measured in EDF-N and EDF-F, and 0.003% in EDF-S are in overdense regions that are more than $3\sigma$ above the SpUDS average surface density.

galaxy sample, the density distributions in the three EDFs and in SpUDS are consistent, and typical of blank fields. Only about 1% (1489 and 1499, respectively) of the densities measured in EDF-N and EDF-F, and 0.003% (1399) in EDF-S are in overdense regions that are more than 3 $\sigma$ above the SpUDS average density.

However, published results of *Spitzer* surface densities reach an IRAC2 magnitude limit more similar to our S2 sample (e.g., Rettura et al. 2014; Wylezalek et al. 2014; Martinache et al. 2018; Mei et al. 2023) than our S1 sample. We compare our S2 surface density measurements within the same radius $(R = 1')$ to those that are publicly available for the CARLA and SpUDS surveys (Wylezalek et al. 2014). The deeper magnitude limit in S2 corresponds to galaxies with $\log_{10}(M_*/M_\odot) \gtrsim 9.5 \pm 0.4$ (see Sect. 4.2).

Figure 4 shows the surface density distributions of our S2 sample in the EDF-N and EDF-F compared to those that we obtain in SpUDS and in the GAEA simulations when applying the same galaxy cuts. Table 3 gives the Gaussian mean and standard deviation of each distribution. The average density distributions and standard deviation of the EDF-N and EDF-F fields are consistent between themselves.

Interestingly, at this deeper magnitude and lower mass limit, 2% (9048) and 3% (9994) of the densities measured in the EDF-N and EDF-F are at 3 $\sigma$ from the SpUDS average density. This is a clear indication that a large part of the less massive galaxies in the two EDFs have larger densities than galaxies with the same mass in the field: there is high potential that they belong to groups or clusters (Wylezalek et al. 2014).

To further illustrate this point, Fig. 5 shows the EDFs surface densities at $> 3\sigma$ from the SpUDS distribution for the EDF-N and EDF-F. These surface densities are comparable to the surface densities observed around the radio-loud AGN at the centres of CARLA clusters. This suggests that our measurements hold promise for detecting cluster and protocluster candidates in

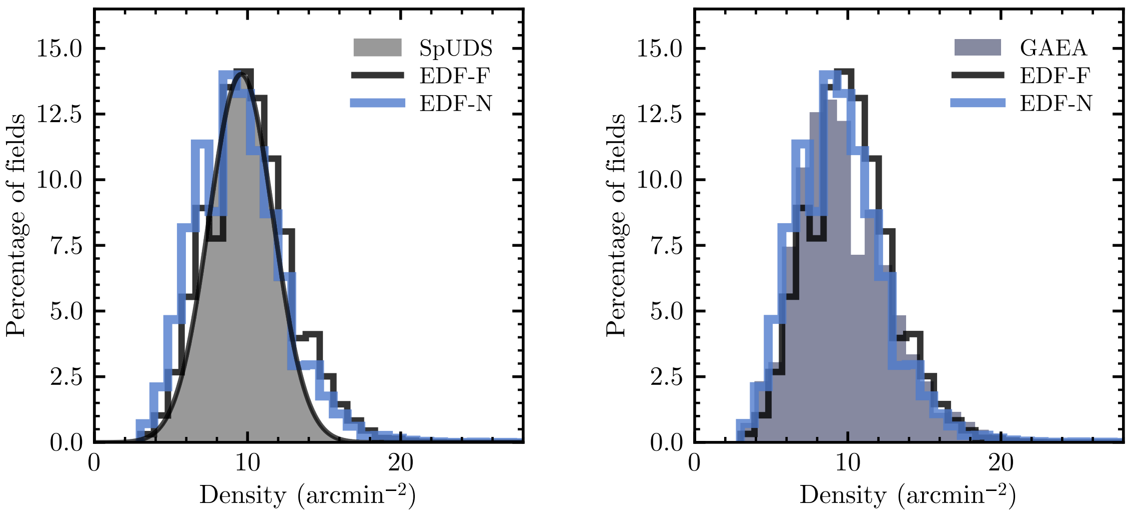


**Fig. 4.** *Spitzer* surface density ($R = 1'$) distributions in EDF-N and EDF-F for our S2 samples, compared to the SpUDS blank field and the GAEA simulations. The SpUDS distribution is shown as a Gaussian. We find that the EDF-N and EDF-F have similar distributions and are consistent with predictions from the GAEA simulations. They, however, have a tail with 2–3% of the galaxies at densities $3\sigma$ higher than the mean.

these fields, as *Spitzer*-selected overdense regions with respect to the field (Wylezalek et al. 2014).

To compare with measurements of surface densities in the GAEA simulation, we degraded the GAEA magnitudes and added uncertainties as described in Sect. 4.3, using as reference the S2 EDF-N *Spitzer* photometry and photometric uncertainties. We then measure densities in the same way as done for the observations. GAEA predictions for the density distribution are consistent with our results.

We note that the GAEA cosmology (Springel et al. 2005) differs from the cosmology adopted in this paper for the $\Sigma_7$ measurements. However, when calculating surface densities we do not use our adopted cosmological parameters, and we do not expect the different GAEA cosmology to substantially impact our results. To test this hypothesis, we compare measurements of $\Sigma_7$ in the degraded GAEA simulations, which do use our adopted cosmological parameters, for two different cosmologies – the Springel et al. (2005) cosmology and the *Planck* 2015 cosmology.

Figure A.1 shows the histogram of $\Sigma_7$ measurements with our chosen cosmology compared to the GAEA cosmology. This comparison demonstrates that the $\Sigma_7$ distributions, assuming the two different cosmologies, are consistent, and therefore we do not expect inconsistencies between our observed aperture measurements and those from GAEA, where cosmology affects in the same way only the galaxy distributions.

### *5.2. Examples of the highest density regions*

As examples illustrating the potential of our measurements, we show the number of passive galaxies found in the 14 highest *Spitzer*-selected surface densities in Table B.3 for the EDF-N and EDF-F. These overdense regions are selected as having S/N> 20 when using all three density measurements. When several densities satisfy this, we keep only the largest density within $2'$. We find that all of the highest-aperture densities in EDF-N have $\Sigma^{\rm pass}_{r>1'} > 3.5\,\sigma$.

We also selected the 10 passive galaxies that have surface densities $> 10\,\sigma$ from the average when using all three density measurements, which are therefore overdense regions of passive galaxies. Again, when several densities satisfy this, we keep only the largest density within $2'$. Table B.4 shows the passive-galaxy overdense regions and their *Spitzer*-selected densities. One of our passive galaxy highest densities, EDF-N ID 1, corresponds to our *Spitzer*-delected highest density EDF-N ID 4.

The presence of passive-galaxy overdense regions and of passive galaxies in *Spitzer*-selected overdense regions is consistent with large fractions of passive galaxies observed in the high-density regions of CARLA clusters (Mei et al. 2023). This is very promising for the future use of our catalogues in the detection of clusters and protoclusters in the EDFs.

We use the Q1 photometric redshifts to estimate the redshift of these extreme densities, with the results given in Tables B.3 and B.4. However, Q1 photometric redshifts have large uncertainties at $z > 1$, and these redshift estimations should be taken with caution. For this reason, we only take galaxies with Q1 photometric redshift uncertainties below 0.5, and we give an estimate of the overdensity average photometric redshift only when we have at least a $3\,\sigma$ peak at a given redshift in the photometric redshift distribution within a circle of $1'$ around our highest *Spitzer*-selected density. The uncertainties in our estimated photometric redshifts are given as the standard deviation of the photometric redshifts within $3\,\sigma$ of the peak redshift in the region. These are very approximate estimations that we will refine when future, more precise, *Euclid* photometric and spectroscopic data releases become available. Figure A.2 shows images of the passive-galaxy highest densities with photometric redshift measurements.

## 6. Cross-correlation with other galaxy ovedense regions in the EDFs

We cross-correlate our *Spitzer* densities with cluster detections from the Q1 cluster catalogue presented in Bhargava et al. (in prep.) at redshifts $z > 1.2$, to take into account Q1 photometric redshift uncertainties. We select *Spitzer* densities within $2'$ of the B25 cluster positions and with $\Sigma_{r<1'}$ at $> 3\sigma$ more than the field average. In EDF-S, we use the S1 catalogue, while we use the S2 catalogues in EDF-N and EDF-F. All cross-identifications are B25 clusters at $z > 1.3$ within the cluster and density photometric redshift uncertainties, except cluster one which has a redshift $z = 1.26 \pm 0.06$. In EDF-S, EDF-N, and EDF-F, we find that

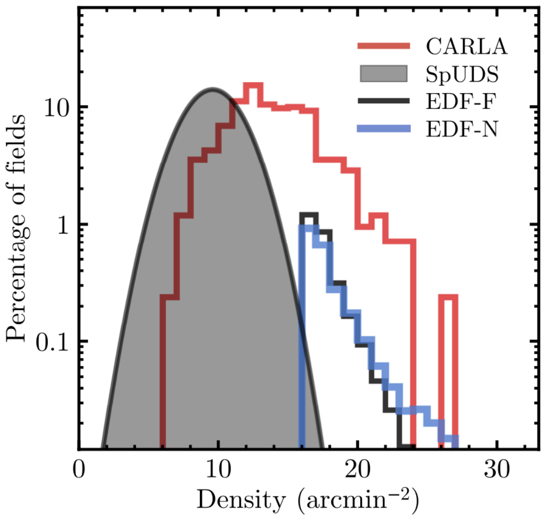


**Fig. 5.** *Spitzer* surface density ($R = 1'$) distributions for the EDF-N and EDF-F S2 sample at $> 3\sigma$ from the field mean, compared to SpUDS and CARLA. This figure demonstrates that the EDF-N and EDF-F show promising high surface densities consistent with those found in CARLA galaxy clusters.

approximately 50%, 30%, and 10%, respectively, of B25 clusters at $z > 1.3$ (within the uncertainties) present *Spitzer*-selected galaxies densities more than $3\sigma$ above the field average.

We also cross-correlate our densities with the SRG/eROSITA All-Sky Survey (eRASS1, Bulbul et al. 2024; Kluge et al. 2024) X-ray cluster catalogue. We do not find eRASS1 clusters at the position of our aperture density measurements that are $> 3\sigma$ with respect to SpUDS. However, this is expected, since we select galaxies at $z > 1.3$, which is higher redshift than the eRASS1 cluster catalogue. It also confirms that our selection is not contaminated by lower redshift massive structures.

## 7. Conclusions

We have combined *Euclid* and *Spitzer* observations of the Q1 EDFs as a basis for extending the detection of *Euclid* clusters and protoclusters to $z > 1.3$. We measured *Spitzer*-selected galaxy densities at $z > 1.3$ and found that 2–3% of the surface densities measured in the EDF-N and EDF-F fall $3\sigma$ above the mean density; these overdense regions are consistent with galaxy densities measured in the CARLA cluster sample at $z > 1.3$.

We also find that the *Spitzer*-selected overdense regions exhibit overdense regions of passive galaxies selected with combined *Euclid* and ancillary DAWN observations. These results confirm the promise of our catalogues for detecting cluster and protocluster candidates in these fields, as *Spitzer*-selected overdense regions with respect to the field (Wylezalek et al. 2014).

We built a catalogue of *Spitzer*-selected galaxy densities at redshift $z > 1.3$ in the EDFs from archival data (Moneti et al. 2022). Source detection was performed with the `SourceExtractor` software, and bright sources were masked to prevent contamination. Our catalogue was validated with the COSMOS2020 catalogue, a data set with a deeper completeness magnitude limit. Using this latter catalogue as a complete reference sample, we found approximately 95% completeness at magnitude limits of IRAC1 = 22.9 and IRAC1 = 23.2 for EDF-N and EDF-N, respectively, and at IRAC1 = 22.4 for the EDF-S.

To measure galaxy densities, we used two complementary methods: (1) aperture and surface density measurements at two different aperture radii ($R = 1'$ and $0\farcm5$); and (2) the $N$th-nearest-neighbour method. Given that *Spitzer* observations in the *Euclid* Q1 fields have different depths, we built two galaxy samples.

– S1, with a magnitude limit of IRAC2 $< 22.2$, at which all EDFs are at least 95% complete; this magnitude limit corresponds to galaxies with $\log_{10}(M_*/M_\odot) \gtrsim 10.0 \pm 0.4$.
– S2, at the depth of IRAC2 $< 22.8$, at which the EDF-N is 95% complete, and which permits us to compare our results to other results already published in the literature; specifically, the CARLA cluster and SpUDS field surveys. This magnitude limit corresponds to galaxies with $\log_{10}(M_*/M_\odot) \gtrsim 9.5 \pm 0.4$.

For the most massive galaxy sample, S1, the density distributions in the three EDFs and in SpUDS are consistent, and typical of blank fields. In fact, only about 1% of the densities measured in EDF-N and EDF-F, and 0.003% in EDF-S, are more than $3\,\sigma$ above the SpUDS average density.

However, when considering the deeper magnitude limit sample, S2, 2% and 3% of the densities measured in the EDF-N and EDF-F, respectively, are at more than $3\,\sigma$ from the SpUDS average density. These overdense regions are characteristic of densities found in CARLA clusters. This is a clear indication that a large part of the less massive galaxies in the two EDFs have larger densities than galaxies with the same mass in the field: there is high potential that they belong to groups or clusters (Wylezalek et al. 2014). We plan a more detailed analysis for cluster and protocluster detection in future work (Mei et al., in prep.).

This result was further confirmed when we measured passive galaxy densities and found passive-galaxy overdense regions in *Spitzer*-selected overdenties. In fact, *Spitzer*-selected clusters and protoclusters in the literature show a high fraction of passive galaxies in their high-density regions out to $z \approx 2$ (Mei et al. 2023).

Our *Spitzer* photometry and density catalogues will be made available upon publication. Table B.5 presents the structure of these final catalogues.

*Acknowledgements.* This work was supported by CNES, focused on the Euclid space mission. NM has received support from France 2030 through the project named Académie Spatiale d'Île-de-France (`https://academiespatiale.fr/`) managed by the National Research Agency under bearing the reference ANR-23-CMAS-0041, and from CNRS/IN2P3. Numerical computations were partly performed on the DANTE platform, APC, France. Based on data from UNIONS, a scientific collaboration using three Hawaii-based telescopes: CFHT, Pan-STARRS, and Subaru `www.skysurvey.cc`. Based on data from the Dark Energy Camera (DECam) on the Blanco 4-m Telescope at CTIO in Chile `https://www.darkenergysurvey.org`. This work is based on observations made with the Spitzer Space Telescope, which was operated by the Jet Propulsion Laboratory, California Institute of Technology under a contract with NASA. Support for this work was provided by NASA through an award issued by JPL/Caltech. This work has made use of the Euclid Quick Release Q1 data from the Euclid mission of the European Space Agency (ESA), 2025, https://doi.org/10.57780/esa-2853f3b. This work has made use of the Early Release Observations (ERO) data from the *Euclid* mission of the European Space Agency (ESA), 2024, `https://doi.org/10.57780/esa-qmocze3`. The Euclid Consortium acknowledges the European Space Agency and a number of agencies and institutes that have supported the development of *Euclid*, in particular the Agenzia Spaziale Italiana, the Austrian Forschungsförderungsgesellschaft funded through BMK, the Belgian Science Policy, the Canadian Euclid Consortium, the Deutsches Zentrum für Luft- und Raumfahrt, the DTU Space and the Niels Bohr Institute in Denmark, the French Centre National d'Etudes Spatiales, the Fundação para a Ciência e a Tecnologia, the Hungarian Academy of Sciences, the Ministerio de Ciencia, Innovación y Universidades, the National Aeronautics and Space Administration, the National Astronomical Observatory of Japan, the Netherlandse Onderzoekschool Voor Astronomie, the Norwegian

Space Agency, the Research Council of Finland, the Romanian Space Agency, the State Secretariat for Education, Research, and Innovation (SERI) at the Swiss Space Office (SSO), and the United Kingdom Space Agency. A complete and detailed list is available on the *Euclid* web site (www.euclid-ec.org). This work has made use of CosmoHub, developed by PIC (maintained by IFAE and CIEMAT) in collaboration with ICE-CSIC. CosmoHub received funding from the Spanish government (MCIN/AEI/10.13039/501100011033), the EU NextGeneration/PRTR (PRTR-C17.I1), and the Generalitat de Catalunya.

## References

Alberts, S., Pope, A., Brodwin, M., et al. 2016, ApJ, 825, 72
Andreon, S., Newman, A. B., Trinchieri, G., et al. 2014, A&A, 565, A120
Aoyama, K., Kodama, T., Suzuki, T. L., et al. 2022, ApJ, 924, 74
Arnouts, S., Le Floc'h, E., Chevallard, J., et al. 2013, A&A, 558, A67
Ascaso, B., Mei, S., Bartlett, J. G., & Benítez, N. 2017, MNRAS, 464, 2270
Baronchelli, I., Scarlata, C., Rodighiero, G., et al. 2016, ApJS, 223, 1
Bertin, E. & Arnouts, S. 1996, A&AS, 117, 393
Brodwin, M., Stanford, S. A., Gonzalez, A. H., et al. 2013, ApJ, 779, 138
Bulbul, E., Liu, A., Kluge, M., et al. 2024, A&A, 685, A106
Casey, C. M. 2016, ApJ, 824, 36
Casey, C. M., Cooray, A., Capak, P., et al. 2015, ApJ, 808, L33
Cooke, E. A., Hatch, N. A., Rettura, A., et al. 2015, MNRAS, 452, 2318
Daddi, E., Jin, S., Strazzullo, V., et al. 2017, ApJ, 846, L31
De Lucia, G. & Blaizot, J. 2007, MNRAS, 375, 2
De Lucia, G., Fontanot, F., Xie, L., & Hirschmann, M. 2024, A&A, 687, A68
Dressler, A. 1980, ApJ, 236, 351
Euclid Collaboration: Aussel, H., Tereno, I., Schirmer, M., et al. 2025, A&A, submitted
Euclid Collaboration: Cleland, C., Mei, S., De Lucia, G., et al. 2025, A&A, submitted
Euclid Collaboration: Cropper, M., Al Bahlawan, A., Amiaux, J., et al. 2024, A&A, accepted, arXiv:2405.13492
Euclid Collaboration: Jahnke, K., Gillard, W., Schirmer, M., et al. 2024, A&A, accepted, arXiv:2405.13493
Euclid Collaboration: Mellier, Y., Abdurro'uf, Acevedo Barroso, J., et al. 2024, A&A, accepted, arXiv:2405.13491
Euclid Collaboration: Romelli, E., Kümmel, M., Dole, H., et al. 2025, A&A, submitted
Euclid Collaboration: Tucci, M., Paltani, S., Hartley, W., et al. 2025, A&A, submitted
Euclid Collaboration: Zalesky, L., McPartland, C. J. R., Weaver, J. R., et al. 2024, arXiv e-prints, arXiv:2408.05296
Fassbender, R., Nastasi, A., Böhringer, H., et al. 2011, A&A, 527, L10
Fazio, G. G., Hora, J. L., Allen, L. E., et al. 2004, ApJS, 154, 10
Franx, M., van Dokkum, P. G., Förster Schreiber, N. M., et al. 2008, ApJ, 688, 770
Galametz, A., Grazian, A., Fontana, A., et al. 2013, ApJS, 206, 10
Gómez, P. L., Nichol, R. C., Miller, C. J., et al. 2003, ApJ, 584, 210
Greenslade, J., Clements, D. L., Cheng, T., et al. 2018, MNRAS, 476, 3336
Gully, H., Hatch, N., Bahé, Y., et al. 2024, MNRAS, 527, 10680
Hatch, N. A., Wylezalek, D., Kurk, J. D., et al. 2014, MNRAS, 445, 280
Hayashi, M., Kodama, T., Koyama, Y., Tadaki, K.-I., & Tanaka, I. 2011, MNRAS, 415, 2670
Hayashi, M., Kodama, T., Tanaka, I., et al. 2016, ApJ, 826, L28
Ji, I., Hasan, I., Schmidt, S. J., & Tyson, J. A. 2018, PASP, 130, 084504
Kelvin, L. S., Hasan, I., & Tyson, J. A. 2023, MNRAS, 520, 2484
Kluge, M., Comparat, J., Liu, A., et al. 2024, A&A, 688, A210
Koyama, Y., Polletta, M. d. C., Tanaka, I., et al. 2021, MNRAS, 503, L1
Kubo, M., Yamada, T., Ichikawa, T., et al. 2017, MNRAS, 469, 2235
Lacy, M., Wilson, G., Masci, F., et al. 2005, ApJS, 161, 41
Lemaux, B. C., Tomczak, A. R., Lubin, L. M., et al. 2019, MNRAS, 490, 1231
Makovoz, D. & Khan, I. 2005, in Astronomical Society of the Pacific Conference Series, Vol. 347, Astronomical Data Analysis Software and Systems XIV, ed. P. Shopbell, M. Britton, & R. Ebert, 81
Markov, V., Mei, S., Salomé, P., et al. 2020, A&A, 641, A22
Martinache, C., Rettura, A., Dole, H., et al. 2018, A&A, 620, A198
Mei, S., Hatch, N. A., Amodeo, S., et al. 2023, A&A, 670, A58
Mei, S., Holden, B. P., Blakeslee, J. P., et al. 2009, ApJ, 690, 42
Mei, S., Scarlata, C., Pentericci, L., et al. 2015, ApJ, 804, 117
Merlin, E., Bourne, N., Castellano, M., et al. 2016, A&A, 595, A97
Merlin, E., Fontana, A., Ferguson, H. C., et al. 2015, A&A, 582, A15
Moneti, A., McCracken, H. J., Shuntov, M., et al. 2022, A&A, 658, A126
Noirot, G., Stern, D., Mei, S., et al. 2018, ApJ, 859, 38
Noirot, G., Vernet, J., De Breuck, C., et al. 2016, ApJ, 830, 90
Oke, J. B. & Gunn, J. E. 1983, ApJ, 266, 713
Papovich, C. 2008, ApJ, 676, 206
Peng, Y.-j., Lilly, S. J., Kovač, K., et al. 2010, ApJ, 721, 193
Peng, Y.-j., Lilly, S. J., Renzini, A., & Carollo, M. 2012, ApJ, 757, 4
Planck Collaboration, Ade, P. A. R., Aghanim, N., et al. 2016, A&A, 594, A13
Polletta, M., Soucail, G., Dole, H., et al. 2021, A&A, 654, A121
Postman, M., Franx, M., Cross, N. J. G., et al. 2005, ApJ, 623, 721
Rettura, A., Chary, R., Krick, J., & Ettori, S. 2018, ApJ, 867, 12
Rettura, A., Martinez-Manso, J., Stern, D., et al. 2014, ApJ, 797, 109
Sartoris, B., Biviano, A., Fedeli, C., et al. 2016, MNRAS, 459, 1764
Sawicki, M. 2002, in American Astronomical Society Meeting Abstracts, Vol. 201, American Astronomical Society Meeting Abstracts, 100.06
Sazonova, E., Alatalo, K., Lotz, J., et al. 2020, ApJ, 899, 85
Shimakawa, R., Koyama, Y., Röttgering, H. J. A., et al. 2018, MNRAS, 481, 5630
Sirianni, M., Jee, M. J., Benítez, N., et al. 2005, PASP, 117, 1049
Springel, V., White, S. D. M., Jenkins, A., et al. 2005, Nature, 435, 629
Stanford, S. A., Eisenhardt, P. R., & Dickinson, M. 1998, ApJ, 492, 461
Strazzullo, V., Coogan, R. T., Daddi, E., et al. 2018, ApJ, 862, 64
Strazzullo, V., Gobat, R., Daddi, E., et al. 2013, ApJ, 772, 118
Tadaki, K.-i., Kodama, T., Ota, K., et al. 2012, MNRAS, 423, 2617
Tran, K.-V. H., Papovich, C., Saintonge, A., et al. 2010, ApJ, 719, L126
van Dokkum, P. G. & van der Marel, R. P. 2007, ApJ, 655, 30
Wainscoat, R. J., Cohen, M., Volk, K., Walker, H. J., & Schwartz, D. E. 1992, ApJS, 83, 111
Wang, T., Elbaz, D., Daddi, E., et al. 2016, ApJ, 828, 56
Weaver, J., Zalesky, L., Allen, N., & Taamoli, S. 2023, The Farmer: Photometry routines for deep multi-wavelength galaxy surveys, Astrophysics Source Code Library, record ascl:2312.016
Weaver, J. R., Kauffmann, O. B., Ilbert, O., et al. 2022, ApJS, 258, 11
Williams, R. J., Quadri, R. F., Franx, M., van Dokkum, P., & Labbé, I. 2009, ApJ, 691, 1879
Wylezalek, D., Galametz, A., Stern, D., et al. 2013, ApJ, 769, 79
Wylezalek, D., Vernet, J., De Breuck, C., et al. 2014, ApJ, 786, 17
Zeimann, G. R., Stanford, S. A., Brodwin, M., et al. 2012, ApJ, 756, 115
Zheng, X. Z., Cai, Z., An, F. X., Fan, X., & Shi, D. D. 2021, MNRAS, 500, 4354

[1] Université Paris Cité, CNRS, Astroparticule et Cosmologie, 75013 Paris, France
[2] CNRS-UCB International Research Laboratory, Centre Pierre Binetruy, IRL2007, CPB-IN2P3, Berkeley, USA
[3] Infrared Processing and Analysis Center, California Institute of Technology, Pasadena, CA 91125, USA
[4] University of California, Los Angeles, CA 90095-1562, USA
[5] INAF-Osservatorio di Astrofisica e Scienza dello Spazio di Bologna, Via Piero Gobetti 93/3, 40129 Bologna, Italy
[6] Instituto de Astrofísica de Canarias (IAC); Departamento de Astrofísica, Universidad de La Laguna (ULL), 38200, La Laguna, Tenerife, Spain
[7] INAF-Osservatorio Astronomico di Trieste, Via G. B. Tiepolo 11, 34143 Trieste, Italy
[8] IFPU, Institute for Fundamental Physics of the Universe, via Beirut 2, 34151 Trieste, Italy
[9] Department of Physics and Astronomy, University of British Columbia, Vancouver, BC V6T 1Z1, Canada
[10] INAF-Osservatorio Astronomico di Brera, Via Brera 28, 20122 Milano, Italy
[11] Université Côte d'Azur, Observatoire de la Côte d'Azur, CNRS, Laboratoire Lagrange, Bd de l'Observatoire, CS 34229, 06304 Nice cedex 4, France
[12] Université Paris-Saclay, CNRS, Institut d'astrophysique spatiale, 91405, Orsay, France
[13] Department of Physics and Astronomy, University of California, Davis, CA 95616, USA
[14] Department of Astronomy, University of Massachusetts, Amherst, MA 01003, USA
[15] Université de Strasbourg, CNRS, Observatoire astronomique de Strasbourg, UMR 7550, 67000 Strasbourg, France
[16] INAF-Osservatorio Astronomico di Brera, Via Brera 28, 20122 Milano, Italy, and INFN-Sezione di Genova, Via Dodecaneso 33, 16146, Genova, Italy
[17] ESAC/ESA, Camino Bajo del Castillo, s/n., Urb. Villafranca del Castillo, 28692 Villanueva de la Cañada, Madrid, Spain
[18] School of Mathematics and Physics, University of Surrey, Guildford, Surrey, GU2 7XH, UK

[19] Université Paris-Saclay, Université Paris Cité, CEA, CNRS, AIM, 91191, Gif-sur-Yvette, France
[20] INFN, Sezione di Trieste, Via Valerio 2, 34127 Trieste TS, Italy
[21] SISSA, International School for Advanced Studies, Via Bonomea 265, 34136 Trieste TS, Italy
[22] Dipartimento di Fisica e Astronomia, Università di Bologna, Via Gobetti 93/2, 40129 Bologna, Italy
[23] INFN-Sezione di Bologna, Viale Berti Pichat 6/2, 40127 Bologna, Italy
[24] INAF-Osservatorio Astronomico di Padova, Via dell'Osservatorio 5, 35122 Padova, Italy
[25] Space Science Data Center, Italian Space Agency, via del Politecnico snc, 00133 Roma, Italy
[26] INAF-Osservatorio Astrofisico di Torino, Via Osservatorio 20, 10025 Pino Torinese (TO), Italy
[27] Dipartimento di Fisica, Università di Genova, Via Dodecaneso 33, 16146, Genova, Italy
[28] INFN-Sezione di Genova, Via Dodecaneso 33, 16146, Genova, Italy
[29] Department of Physics "E. Pancini", University Federico II, Via Cinthia 6, 80126, Napoli, Italy
[30] INAF-Osservatorio Astronomico di Capodimonte, Via Moiariello 16, 80131 Napoli, Italy
[31] Instituto de Astrofísica e Ciências do Espaço, Universidade do Porto, CAUP, Rua das Estrelas, PT4150-762 Porto, Portugal
[32] Faculdade de Ciências da Universidade do Porto, Rua do Campo de Alegre, 4150-007 Porto, Portugal
[33] Aix-Marseille Université, CNRS, CNES, LAM, Marseille, France
[34] Dipartimento di Fisica, Università degli Studi di Torino, Via P. Giuria 1, 10125 Torino, Italy
[35] INFN-Sezione di Torino, Via P. Giuria 1, 10125 Torino, Italy
[36] European Space Agency/ESTEC, Keplerlaan 1, 2201 AZ Noordwijk, The Netherlands
[37] Institute Lorentz, Leiden University, Niels Bohrweg 2, 2333 CA Leiden, The Netherlands
[38] Leiden Observatory, Leiden University, Einsteinweg 55, 2333 CC Leiden, The Netherlands
[39] INAF-IASF Milano, Via Alfonso Corti 12, 20133 Milano, Italy
[40] Centro de Investigaciones Energéticas, Medioambientales y Tecnológicas (CIEMAT), Avenida Complutense 40, 28040 Madrid, Spain
[41] Port d'Informació Científica, Campus UAB, C. Albareda s/n, 08193 Bellaterra (Barcelona), Spain
[42] Institute for Theoretical Particle Physics and Cosmology (TTK), RWTH Aachen University, 52056 Aachen, Germany
[43] INAF-Osservatorio Astronomico di Roma, Via Frascati 33, 00078 Monteporzio Catone, Italy
[44] INFN section of Naples, Via Cinthia 6, 80126, Napoli, Italy
[45] Institute for Astronomy, University of Hawaii, 2680 Woodlawn Drive, Honolulu, HI 96822, USA
[46] Dipartimento di Fisica e Astronomia "Augusto Righi" - Alma Mater Studiorum Università di Bologna, Viale Berti Pichat 6/2, 40127 Bologna, Italy
[47] Instituto de Astrofísica de Canarias, Vía Láctea, 38205 La Laguna, Tenerife, Spain
[48] Institute for Astronomy, University of Edinburgh, Royal Observatory, Blackford Hill, Edinburgh EH9 3HJ, UK
[49] Jodrell Bank Centre for Astrophysics, Department of Physics and Astronomy, University of Manchester, Oxford Road, Manchester M13 9PL, UK
[50] European Space Agency/ESRIN, Largo Galileo Galilei 1, 00044 Frascati, Roma, Italy
[51] Université Claude Bernard Lyon 1, CNRS/IN2P3, IP2I Lyon, UMR 5822, Villeurbanne, F-69100, France
[52] Institut de Ciències del Cosmos (ICCUB), Universitat de Barcelona (IEEC-UB), Martí i Franquès 1, 08028 Barcelona, Spain
[53] Institució Catalana de Recerca i Estudis Avançats (ICREA), Passeig de Lluís Companys 23, 08010 Barcelona, Spain
[54] UCB Lyon 1, CNRS/IN2P3, IUF, IP2I Lyon, 4 rue Enrico Fermi, 69622 Villeurbanne, France
[55] Departamento de Física, Faculdade de Ciências, Universidade de Lisboa, Edifício C8, Campo Grande, PT1749-016 Lisboa, Portugal
[56] Instituto de Astrofísica e Ciências do Espaço, Faculdade de Ciências, Universidade de Lisboa, Campo Grande, 1749-016 Lisboa, Portugal
[57] Department of Astronomy, University of Geneva, ch. d'Ecogia 16, 1290 Versoix, Switzerland
[58] INAF-Istituto di Astrofisica e Planetologia Spaziali, via del Fosso del Cavaliere, 100, 00100 Roma, Italy
[59] INFN-Padova, Via Marzolo 8, 35131 Padova, Italy
[60] Aix-Marseille Université, CNRS/IN2P3, CPPM, Marseille, France
[61] INFN-Bologna, Via Irnerio 46, 40126 Bologna, Italy
[62] Institut d'Estudis Espacials de Catalunya (IEEC), Edifici RDIT, Campus UPC, 08860 Castelldefels, Barcelona, Spain
[63] Institute of Space Sciences (ICE, CSIC), Campus UAB, Carrer de Can Magrans, s/n, 08193 Barcelona, Spain
[64] School of Physics, HH Wills Physics Laboratory, University of Bristol, Tyndall Avenue, Bristol, BS8 1TL, UK
[65] Universitäts-Sternwarte München, Fakultät für Physik, Ludwig-Maximilians-Universität München, Scheinerstrasse 1, 81679 München, Germany
[66] Max Planck Institute for Extraterrestrial Physics, Giessenbachstr. 1, 85748 Garching, Germany
[67] Institute of Theoretical Astrophysics, University of Oslo, P.O. Box 1029 Blindern, 0315 Oslo, Norway
[68] Jet Propulsion Laboratory, California Institute of Technology, 4800 Oak Grove Drive, Pasadena, CA, 91109, USA
[69] Felix Hormuth Engineering, Goethestr. 17, 69181 Leimen, Germany
[70] Technical University of Denmark, Elektrovej 327, 2800 Kgs. Lyngby, Denmark
[71] Cosmic Dawn Center (DAWN), Denmark
[72] Institut d'Astrophysique de Paris, UMR 7095, CNRS, and Sorbonne Université, 98 bis boulevard Arago, 75014 Paris, France
[73] Max-Planck-Institut für Astronomie, Königstuhl 17, 69117 Heidelberg, Germany
[74] NASA Goddard Space Flight Center, Greenbelt, MD 20771, USA
[75] Department of Physics and Helsinki Institute of Physics, Gustaf Hällströmin katu 2, 00014 University of Helsinki, Finland
[76] Université de Genève, Département de Physique Théorique and Centre for Astroparticle Physics, 24 quai Ernest-Ansermet, CH-1211 Genève 4, Switzerland
[77] Department of Physics, P.O. Box 64, 00014 University of Helsinki, Finland
[78] Helsinki Institute of Physics, Gustaf Hällströmin katu 2, University of Helsinki, Helsinki, Finland
[79] Centre de Calcul de l'IN2P3/CNRS, 21 avenue Pierre de Coubertin 69627 Villeurbanne Cedex, France
[80] Laboratoire d'etude de l'Univers et des phenomenes eXtremes, Observatoire de Paris, Université PSL, Sorbonne Université, CNRS, 92190 Meudon, France
[81] SKA Observatory, Jodrell Bank, Lower Withington, Macclesfield, Cheshire SK11 9FT, UK
[82] Dipartimento di Fisica "Aldo Pontremoli", Università degli Studi di Milano, Via Celoria 16, 20133 Milano, Italy
[83] INFN-Sezione di Milano, Via Celoria 16, 20133 Milano, Italy
[84] Universität Bonn, Argelander-Institut für Astronomie, Auf dem Hügel 71, 53121 Bonn, Germany
[85] INFN-Sezione di Roma, Piazzale Aldo Moro, 2 - c/o Dipartimento di Fisica, Edificio G. Marconi, 00185 Roma, Italy
[86] Dipartimento di Fisica e Astronomia "Augusto Righi" - Alma Mater Studiorum Università di Bologna, via Piero Gobetti 93/2, 40129 Bologna, Italy
[87] Department of Physics, Institute for Computational Cosmology, Durham University, South Road, Durham, DH1 3LE, UK
[88] Institut d'Astrophysique de Paris, 98bis Boulevard Arago, 75014, Paris, France
[89] Institute of Physics, Laboratory of Astrophysics, Ecole Polytechnique Fédérale de Lausanne (EPFL), Observatoire de Sauverny, 1290 Versoix, Switzerland

[90] Aurora Technology for European Space Agency (ESA), Camino bajo del Castillo, s/n, Urbanizacion Villafranca del Castillo, Villanueva de la Cañada, 28692 Madrid, Spain
[91] Institut de Física d'Altes Energies (IFAE), The Barcelona Institute of Science and Technology, Campus UAB, 08193 Bellaterra (Barcelona), Spain
[92] School of Mathematics, Statistics and Physics, Newcastle University, Herschel Building, Newcastle-upon-Tyne, NE1 7RU, UK
[93] DARK, Niels Bohr Institute, University of Copenhagen, Jagtvej 155, 2200 Copenhagen, Denmark
[94] Waterloo Centre for Astrophysics, University of Waterloo, Waterloo, Ontario N2L 3G1, Canada
[95] Department of Physics and Astronomy, University of Waterloo, Waterloo, Ontario N2L 3G1, Canada
[96] Perimeter Institute for Theoretical Physics, Waterloo, Ontario N2L 2Y5, Canada
[97] Centre National d'Etudes Spatiales – Centre spatial de Toulouse, 18 avenue Edouard Belin, 31401 Toulouse Cedex 9, France
[98] Institute of Space Science, Str. Atomistilor, nr. 409 Măgurele, Ilfov, 077125, Romania
[99] Dipartimento di Fisica e Astronomia "G. Galilei", Università di Padova, Via Marzolo 8, 35131 Padova, Italy
[100] Institut für Theoretische Physik, University of Heidelberg, Philosophenweg 16, 69120 Heidelberg, Germany
[101] Institut de Recherche en Astrophysique et Planétologie (IRAP), Université de Toulouse, CNRS, UPS, CNES, 14 Av. Edouard Belin, 31400 Toulouse, France
[102] Université St Joseph; Faculty of Sciences, Beirut, Lebanon
[103] Departamento de Física, FCFM, Universidad de Chile, Blanco Encalada 2008, Santiago, Chile
[104] Satlantis, University Science Park, Sede Bld 48940, Leioa-Bilbao, Spain
[105] Instituto de Astrofísica e Ciências do Espaço, Faculdade de Ciências, Universidade de Lisboa, Tapada da Ajuda, 1349-018 Lisboa, Portugal
[106] Universidad Politécnica de Cartagena, Departamento de Electrónica y Tecnología de Computadoras, Plaza del Hospital 1, 30202 Cartagena, Spain
[107] Kapteyn Astronomical Institute, University of Groningen, PO Box 800, 9700 AV Groningen, The Netherlands
[108] Dipartimento di Fisica e Scienze della Terra, Università degli Studi di Ferrara, Via Giuseppe Saragat 1, 44122 Ferrara, Italy
[109] Istituto Nazionale di Fisica Nucleare, Sezione di Ferrara, Via Giuseppe Saragat 1, 44122 Ferrara, Italy
[110] INAF, Istituto di Radioastronomia, Via Piero Gobetti 101, 40129 Bologna, Italy
[111] Department of Physics, Oxford University, Keble Road, Oxford OX1 3RH, UK
[112] INAF - Osservatorio Astronomico di Brera, via Emilio Bianchi 46, 23807 Merate, Italy
[113] ICL, Junia, Université Catholique de Lille, LITL, 59000 Lille, France
[114] ICSC - Centro Nazionale di Ricerca in High Performance Computing, Big Data e Quantum Computing, Via Magnanelli 2, Bologna, Italy
[115] Instituto de Física Teórica UAM-CSIC, Campus de Cantoblanco, 28049 Madrid, Spain
[116] CERCA/ISO, Department of Physics, Case Western Reserve University, 10900 Euclid Avenue, Cleveland, OH 44106, USA
[117] Technical University of Munich, TUM School of Natural Sciences, Physics Department, James-Franck-Str. 1, 85748 Garching, Germany
[118] Max-Planck-Institut für Astrophysik, Karl-Schwarzschild-Str. 1, 85748 Garching, Germany
[119] Laboratoire Univers et Théorie, Observatoire de Paris, Université PSL, Université Paris Cité, CNRS, 92190 Meudon, France
[120] Departamento de Física Fundamental. Universidad de Salamanca. Plaza de la Merced s/n. 37008 Salamanca, Spain
[121] Center for Data-Driven Discovery, Kavli IPMU (WPI), UTIAS, The University of Tokyo, Kashiwa, Chiba 277-8583, Japan
[122] Ludwig-Maximilians-University, Schellingstrasse 4, 80799 Munich, Germany
[123] Max-Planck-Institut für Physik, Boltzmannstr. 8, 85748 Garching, Germany
[124] Dipartimento di Fisica - Sezione di Astronomia, Università di Trieste, Via Tiepolo 11, 34131 Trieste, Italy
[125] California Institute of Technology, 1200 E California Blvd, Pasadena, CA 91125, USA
[126] Department of Physics & Astronomy, University of California Irvine, Irvine CA 92697, USA
[127] Department of Mathematics and Physics E. De Giorgi, University of Salento, Via per Arnesano, CP-I93, 73100, Lecce, Italy
[128] INFN, Sezione di Lecce, Via per Arnesano, CP-193, 73100, Lecce, Italy
[129] INAF-Sezione di Lecce, c/o Dipartimento Matematica e Fisica, Via per Arnesano, 73100, Lecce, Italy
[130] Departamento Física Aplicada, Universidad Politécnica de Cartagena, Campus Muralla del Mar, 30202 Cartagena, Murcia, Spain
[131] Instituto de Física de Cantabria, Edificio Juan Jordá, Avenida de los Castros, 39005 Santander, Spain
[132] Observatorio Nacional, Rua General Jose Cristino, 77-Bairro Imperial de Sao Cristovao, Rio de Janeiro, 20921-400, Brazil
[133] CEA Saclay, DFR/IRFU, Service d'Astrophysique, Bat. 709, 91191 Gif-sur-Yvette, France
[134] Institute of Cosmology and Gravitation, University of Portsmouth, Portsmouth PO1 3FX, UK
[135] Department of Astronomy, University of Florida, Bryant Space Science Center, Gainesville, FL 32611, USA
[136] Department of Computer Science, Aalto University, PO Box 15400, Espoo, FI-00 076, Finland
[137] Instituto de Astrofísica de Canarias, c/ Via Lactea s/n, La Laguna 38200, Spain. Departamento de Astrofísica de la Universidad de La Laguna, Avda. Francisco Sanchez, La Laguna, 38200, Spain
[138] Universidad de La Laguna, Departamento de Astrofísica, 38206 La Laguna, Tenerife, Spain
[139] Ruhr University Bochum, Faculty of Physics and Astronomy, Astronomical Institute (AIRUB), German Centre for Cosmological Lensing (GCCL), 44780 Bochum, Germany
[140] Department of Physics and Astronomy, Vesilinnantie 5, 20014 University of Turku, Finland
[141] Serco for European Space Agency (ESA), Camino bajo del Castillo, s/n, Urbanizacion Villafranca del Castillo, Villanueva de la Cañada, 28692 Madrid, Spain
[142] ARC Centre of Excellence for Dark Matter Particle Physics, Melbourne, Australia
[143] Centre for Astrophysics & Supercomputing, Swinburne University of Technology, Hawthorn, Victoria 3122, Australia
[144] Department of Physics and Astronomy, University of the Western Cape, Bellville, Cape Town, 7535, South Africa
[145] DAMTP, Centre for Mathematical Sciences, Wilberforce Road, Cambridge CB3 0WA, UK
[146] Kavli Institute for Cosmology Cambridge, Madingley Road, Cambridge, CB3 0HA, UK
[147] Department of Astrophysics, University of Zurich, Winterthurerstrasse 190, 8057 Zurich, Switzerland
[148] Department of Physics, Centre for Extragalactic Astronomy, Durham University, South Road, Durham, DH1 3LE, UK
[149] IRFU, CEA, Université Paris-Saclay 91191 Gif-sur-Yvette Cedex, France
[150] Oskar Klein Centre for Cosmoparticle Physics, Department of Physics, Stockholm University, Stockholm, SE-106 91, Sweden
[151] Astrophysics Group, Blackett Laboratory, Imperial College London, London SW7 2AZ, UK
[152] Univ. Grenoble Alpes, CNRS, Grenoble INP, LPSC-IN2P3, 53, Avenue des Martyrs, 38000, Grenoble, France
[153] INAF-Osservatorio Astrofisico di Arcetri, Largo E. Fermi 5, 50125, Firenze, Italy
[154] Dipartimento di Fisica, Sapienza Università di Roma, Piazzale Aldo Moro 2, 00185 Roma, Italy

[155] Centro de Astrofísica da Universidade do Porto, Rua das Estrelas, 4150-762 Porto, Portugal
[156] HE Space for European Space Agency (ESA), Camino bajo del Castillo, s/n, Urbanizacion Villafranca del Castillo, Villanueva de la Cañada, 28692 Madrid, Spain
[157] Department of Astrophysical Sciences, Peyton Hall, Princeton University, Princeton, NJ 08544, USA
[158] Theoretical astrophysics, Department of Physics and Astronomy, Uppsala University, Box 515, 751 20 Uppsala, Sweden
[159] Minnesota Institute for Astrophysics, University of Minnesota, 116 Church St SE, Minneapolis, MN 55455, USA
[160] Mathematical Institute, University of Leiden, Einsteinweg 55, 2333 CA Leiden, The Netherlands
[161] School of Physics & Astronomy, University of Southampton, Highfield Campus, Southampton SO17 1BJ, UK
[162] Institute of Astronomy, University of Cambridge, Madingley Road, Cambridge CB3 0HA, UK
[163] Space physics and astronomy research unit, University of Oulu, Pentti Kaiteran katu 1, FI-90014 Oulu, Finland
[164] Center for Computational Astrophysics, Flatiron Institute, 162 5th Avenue, 10010, New York, NY, USA

## Appendix A: Figures

Figure A.1 shows the number count distribution of $\Sigma_7$ densities in the GAEA simulations for two different cosmologies: the Planck Collaboration et al. (2016) cosmology and the *Millennium* simulation cosmology (Springel et al. 2005). The two distributions are consistent. This means that the choice of cosmology should not impact our results.

Figure A.2 shows examples of our *Spitzer*-selected highest-density regions with high densities of passive galaxies, presented in Table B.4.

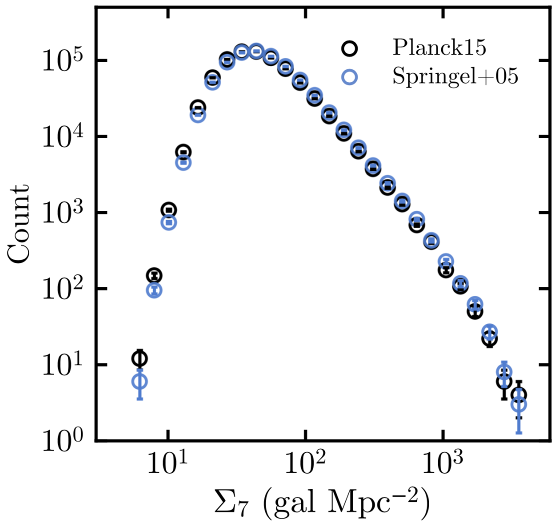


**Fig. A.1.** Number count distribution of $\Sigma_7$ densities in GAEA for both the Planck Collaboration et al. (2016) cosmology and the *Millennium* simulation cosmology (Springel et al. 2005). Poisson errors are included as error bars. The two distributions are consistent within their mutual uncertainties, indicating that the choice of cosmology should not impact our results.

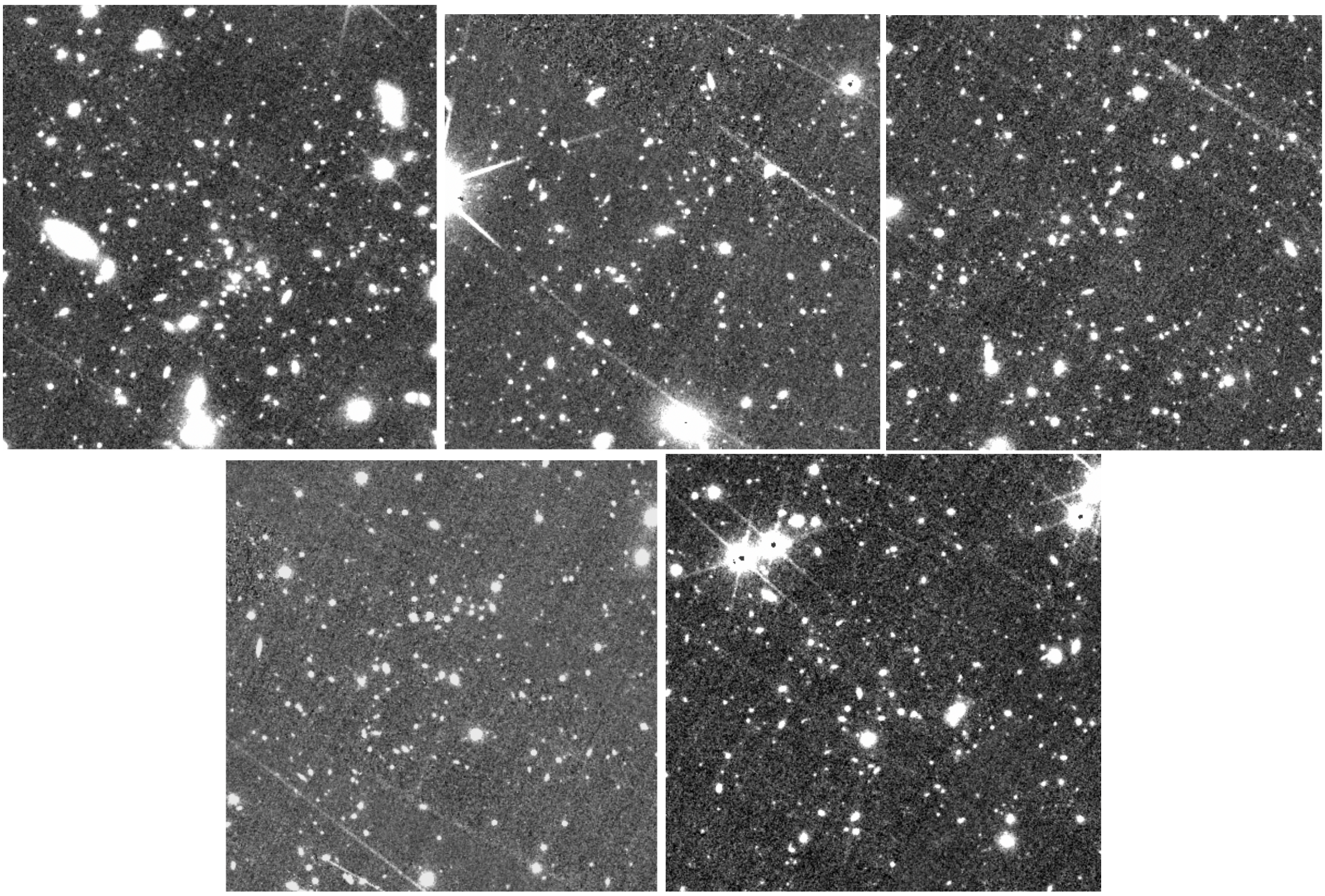

**Fig. A.2.** Examples of our *Spitzer*-selected highest-density regions with high densities of passive galaxies. The size of each image is $2' \times 2'$. From left to right and top to bottom: density ID 1, 3, 9, 2, 4, at redshift 1.39 ± 0.05, 1.39 ± 0.05, 1.39 ± 0.05, 1.46 ± 0.04, and 1.54 ± 0.06, respectively, as from Table B.4.

## Appendix B: Tables

Table B.1 shows the SourceExtractor key parameters used for source detection when performing IRAC photometry.

Table B.2 shows the parameters used when performing IRAC photometry using t-phot (Merlin et al. 2015, 2016). The t-phot pipeline consists of several steps and works the best when running two passes. The first pass (1pass) (1) creates multiwavelength stamps for the galaxies in the input catalogue of the high-resolution image (priors); (2) then convolves these stamps with a kernel that reduces the stamps to the low-resolution image (convolve); (3) performs the fitting procedure to model each source flux in the low-resolution image (fit); (4) chooses the best fit (diags); (5) computes a list of positional shifts, and a set of shifted kernels are generated and stored (dance).The second pass repeats steps (2), (3) and (4) above, and then archives the results (archive). In the priors stage, we can choose to use observed pixel values (usereal), which is what we do, or a model (usemodels) or indicate that we have unresolved sources (useunresolved). If the convolution is performed in the Fourier space, which is our case, the parameter FFTconv is set as true. In the fitting stage, we: (1) use the cells-on-object algorithm (coo), for which an optimized number of objects is considered in a cell to minimize bias; (2) activate as true the cellmask option, which excludes pixels from the fit if they are below a given floor (maskfloor); (3) do not fit the background (fitbackground); (4) do not apply a threshold (threshold) that defines the pixels above it that are used in the fitting process; (5) choose the Cholesky solution method (lu); (6) and exclude negative solutions (clip). For details on each step, please refer to Merlin et al. (2015, 2016).

Table B.3 shows examples of our S2 *Spitzer*-selected highest-density regions. Table B.4 presents the ten largest passive-galaxy densities in EDF-N. Table B.5 shows the structure of our catalogues of *Spitzer* photometry and projected galaxy densities.

**Table B.1.** SourceExtractor key parameters used for source detection in all fields.

| Parameter | Value |
|---|---|
| DETECT_MINAREA | 3.0 |
| DETECT_THRESH | 1.8 |
| ANALYSIS_THRESH | 1.8 |
| DEBLEND_NTHRESH | 32 |
| DEBLEND_MINCONT | 0.0001 |
| BACK_SIZE | 16 |
| BACK_FILTERSIZE | 3 |
| BACKPHOTO_THICK | 32 |
| BACKPHOTO_TYPE | LOCAL |

**Table B.2.** `t-phot` parameters.

| | | |
|---|---|---|
| Pipeline | 1st pass | priors, convolve, fit, diags, dance |
| | 2nd pass | convolve, fit, diags, archive |
| Priors stage | usereal | true |
| | usemodels | false |
| | useunresolved | false |
| Convolution stage | FFTconv | true |
| Fitting stage | fitting | coo |
| | cellmask | true |
| | maskfloor | $10^{-9}$ |
| | fitbackground | false |
| | threshold | 0.0 |
| | linsyssolver | lu |
| | clip | true |

**Table B.3.** Examples of our S2 *Spitzer*-selected highest-density regions. These have been selected as having densities > 20 $\sigma$ with all our three methods.

| Q1 Field | ID | RA | Dec | $z_{\rm phot}$ | $N_{\rm zphot}$ | $N^{\rm pass}(r<1')$ | $\Sigma_{(r<1')}$ | $S/N_{(r<1')}$ | $\Sigma_7$ | $S/N_{\Sigma_7}$ |
|---|---|---|---|---|---|---|---|---|---|---|
| EDF-N | 1 | 272.13150 | +67.17863 | | | 4 | 5 | 25 | 288 | 130 |
| EDF-N | 2 | 268.59576 | +64.89498 | | | 7 | 5 | 24 | 170 | 76 |
| EDF-N | 3 | 270.68832 | +65.35073 | | | 4 | 5 | 23 | 225 | 100 |
| EDF-N | 4 | 266.79734 | +65.54727 | $1.39 \pm 0.03$ | 57 | 15 | 5 | 23 | 181 | 80 |
| EDF-N | 5 | 270.82411 | +65.06381 | $1.36 \pm 0.02$ | 56 | 6 | 5 | 22 | 168 | 75 |
| EDF-N | 6 | 270.11342 | +66.25161 | $1.46 \pm 0.02$ | 56 | 9 | 5 | 22 | 257 | 120 |
| EDF-N | 7 | 272.93821 | +67.03152 | | | 8 | 5 | 23 | 161 | 70 |
| EDF-N | 8 | 267.37057 | +66.53104 | | | 4 | 5 | 21 | 332 | 150 |
| EDF-N | 9 | 269.59719 | +64.65159 | | | 6 | 5 | 21 | 157 | 70 |
| EDF-N | 10 | 266.85880 | +65.72311 | | | 8 | 5 | 21 | 145 | 64 |
| EDF-F | 11 | 52.33491 | −28.50047 | | | | 6 | 25 | 216 | 100 |
| EDF-F | 12 | 51.60704 | −27.17787 | | | | 5 | 24 | 230 | 100 |
| EDF-F | 13 | 54.14683 | −28.59636 | | | | 5 | 22 | 192 | 90 |
| EDF-F | 14 | 51.92977 | −27.67554 | | | | 5 | 21 | 214 | 100 |

**Notes.** The columns are: Q1 field indicates the EDFs hosting the densities; ID is the density ID; right ascension, RA, and declination, Dec, give the position; $z_{\rm phot}$ is an estimate of the redshift from the Q1 photometric redshift release (see text); $N_{\rm zphot}$ is the number of galaxies used for the photometric redshift estimate (see text); $N_{\rm pass}$ is the number of selected passive galaxies within a $1'$ radius aperture from the *Spitzer*-selected density; $\Sigma_{r<R'}$ is the aperture density and $S/N_{r<R'}$ is its S/N; $\Sigma_7$ is the density calculated with the *N*th-nearest-neighbour method in units of galaxies per $Mpc^2$ and $S/N_7$ is its S/N. We remind the reader that we can select passive galaxies only in EDF-N, and this is why we don't find passive overdense regions in EDF-F.

**Table B.4.** The ten largest passive-galaxy densities in EDF-N, with densities > 10 $\sigma$ from the average.

| Q1 Field | ID | RA | Dec | $z_{\rm phot}$ | $N_{\rm zphot}$ | $N^{\rm pass}(r<1')$ | $\Sigma^{\rm pass}_{(r<1')}$ | $\rm S/N^{pass}_{(r<1')}$ | $\Sigma^{\rm pass}_{7}$ | $\rm S/N^{pass}_{\Sigma_7}$ |
|---|---|---|---|---|---|---|---|---|---|---|
| EDF-N | 1 | 266.80351 | +65.55044 | 1.39 ± 0.05 | 15 | 15 | 6 | 13 | 6 ± 2 | 30 |
| EDF-N | 2 | 266.88792 | +66.06646 | 1.46 ± 0.04 | 13 | 13 | 5 | 11 | 4 ± 2 | 20 |
| EDF-N | 3 | 267.48010 | +66.07398 | 1.39 ± 0.05 | 12 | 17 | 7 | 15 | 6 ± 2 | 30 |
| EDF-N | 4 | 267.68164 | +67.30834 | 1.54 ± 0.06 | 11 | 13 | 5 | 11 | 4 ± 2 | 20 |
| EDF-N | 5 | 267.85836 | +66.36558 | | | 14 | 6 | 12 | 8 ± 3 | 40 |
| EDF-N | 6 | 268.47776 | +64.88699 | | | 13 | 5 | 11 | 3 ± 1 | 10 |
| EDF-N | 7 | 268.79228 | +67.69032 | | | 15 | 6 | 13 | 9 ± 4 | 45 |
| EDF-N | 8 | 269.39637 | +65.22664 | | | 15 | 6 | 13 | 3 ± 1 | 14 |
| EDF-N | 9 | 271.82177 | +65.49944 | 1.39 ± 0.05 | 12 | 13 | 5 | 11 | 3 ± 1 | 14 |
| EDF-N | 10 | 271.99077 | +65.71248 | | | 13 | 5 | 11 | 4± 2 | 20 |

**Notes.** The columns are: Q1 field indicates the EDFs hosting densities; ; ID is the density ID; right ascension, RA, and declination, Dec, give the position; $z_{\rm phot}$ is an estimate of the redshift from the Q1 photometric redshift release (see text); $N_{\rm zphot}$ is the number of galaxies used for the photometric redshift estimate (see text); $N_{\rm pass}$ is the number of selected passive galaxies within a $1'$radius aperture from the *Spitzer*-selected density; $\Sigma^{\rm pass}_{r<R'}$ is the aperture density of passive galaxies and $\rm SNR^{pass}_{r<R'}$ its S/N; $\Sigma^{\rm pass}_{7}$ is the passive galaxy density calculated with the *N*th-nearest-neighbour method in units of galaxies per Mpc$^2$ and $\rm SNR^{pass}_{7}$ its S/N.

**Table B.5.** *Spitzer* photometry and projected galaxy densities: catalogue column structure

| Q1 field | Cluster ID | RA | Dec | $z_{\rm phot}$ | $\Sigma^{\rm max}_{7}$ | $N^{\rm max}_{1'}$ | $\rm S/N^{N}_{(r<1')}$ | $N^{\rm max}_{(r<0.5')}$ | $\rm S/N^{N}_{(r<0.5')}$ |
|---|---|---|---|---|---|---|---|---|---|
| EDFN | 266.88946 | +66.06738 | ... | .. | .. | ... | ... | ... | ... |
| EDFN | 270.88027 | +65.72358 | ... | .. | .. | ... | ... | ... | ... |
| EDFN | 267.36383 | +66.52386 | ... | .. | .. | ... | ... | ... | ... |

**Notes.** The columns are: Q1 field indicates the EDFs hosting the densities; right ascension, RA, and declination, Dec, give the position; $\Sigma_7$ is the density calculated with the *N*th-nearest-neighbour method in units of galaxies per Mpc$^2$ and $\rm SNR_7$ its S/N; $\Sigma_{r<R'}$ is the aperture density and $\rm SNR_{r<R'}$ its S/N.